

## Supporting Information

*Exciton Delocalization and Scaffold Stability in Bridged Nucleotide-substituted, DNA Duplex-templated Cyanine Aggregates*

Authors: <sup>1</sup>Simon K. Roy; <sup>1</sup>Olga A. Mass; <sup>1</sup>Donald L. Kellis; <sup>1</sup>Christopher K. Wilson; <sup>2</sup>John A. Hall;  
<sup>\*1,3</sup>Bernard Yurke; and <sup>\*1,3</sup>William B. Knowlton

<sup>1</sup>Micron School of Materials Science and Engineering, <sup>2</sup>Division of Research and Economic Development,  
<sup>3</sup>Department of Electrical & Computer Engineering, Boise State University, Boise, Idaho, 83725, United States

Corresponding authors:

\*[bernardyurke@boisestate.edu](mailto:bernardyurke@boisestate.edu)

\*[bknowlton@boisestate.edu](mailto:bknowlton@boisestate.edu)

Table of contents

S11	Melting Curves	S2
S12	Polyacrylamide Gel Electrophoresis	S17
S13	Theoretical Modeling with the KRM Model Simulation Tool	S22
S14	Vibrational coupling in Steady-State Optical Spectra	S43
S15	Ultra-violet Circular Dichroism	S48
S16	Steady-State Fluorescence	S50
S17	References	S52

### S11: Melting Curves

Temperature-dependent absorbance experiments were performed for all samples by monitoring absorbance at 260 nm as a function of temperature using a Cary-5000 UV-Vis-near-infrared (NIR) spectrophotometer (Agilent). Samples were degassed under vacuum at room temperature and transferred to a capped low-headspace cuvette (40  $\mu$ L; Starna). Temperature was increased at a rate of 1  $^{\circ}$ C/min from 25  $^{\circ}$ C to 98  $^{\circ}$ C while collecting a data point every 0.25  $^{\circ}$ C from 60  $^{\circ}$ C to 98  $^{\circ}$ C with a 3-second accumulation time and a 2-nm slit width. Thermal denaturation temperatures were determined by fitting the derivative of absorbance with respect to temperature with one or more Gaussian curves (**Figures S1-S5**). Fitting with a single Gaussian curve results in a peak maximum that corresponds to the inflection point of the absorbance versus temperature data. In these cases, the melting transition was assigned to the temperature corresponding to the peak of the single Gaussian. If a sum of two Gaussian curves was needed to fit the data, the center of the lower temperature curve was assigned to a minor “pre-melting” transition, whereas the higher temperature curve was assigned to the main melting transition.

The derivative of the unlabeled DNA:DNA sample data were well-described by a single Gaussian curve indicating a single cooperative melting event. Substitution of seven nucleotides, either LNA or BNA, on one strand of the 42 base-pair (bp) duplex resulted in a significant increase in melting temperature. Chromophore-labeled samples required an additional fitting curve centered at a lower temperature, which were assigned to “pre-melting” events. Results are summarized in **Table S1**.

Although the approach to fitting the melting data and extracting the melting points is empirical and to first order, the trends revealed by this analysis are clear. Melting transition temperatures for both pre-melting and main melting transitions decreased as the number of inserted chromophores increased. In every case, however, the destabilization was partially mitigated by stabilizing effects from inclusion of bridged nucleic analogs. In all cases, samples containing LNA or BNA showed an increase melting temperature compared with corresponding DNA-only samples. The stabilizing effect of the LNA and BNA decreased as the number of chromophores increased. We hypothesize that the diminishing stabilization is due to the domain of the LNA/BNA being increasingly destabilized with each additional chromophore such that fewer LNA or BNA nucleotides are properly hybridized and stacked in a well-formed double helix.

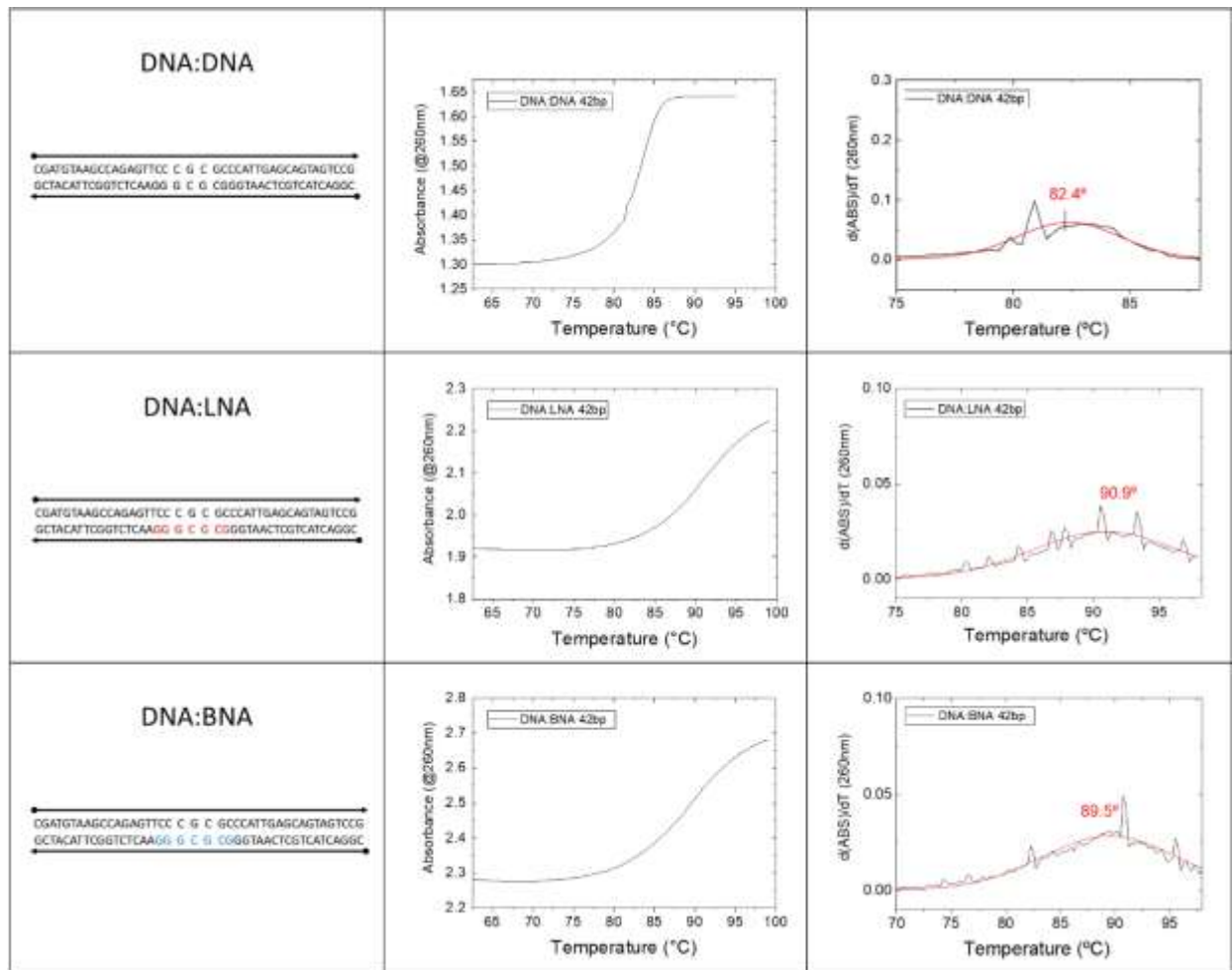


**Figure S1:** Schematics for unlabeled samples (left) with temperature-dependent absorbance at 260nm (center) and the first derivative with respect to temperature (right). Derivative curves were decomposed into one or more Gaussian profiles using Origin Pro (2019b). Temperatures for pre-melting (green) and main (red) melting transitions were determined by noting the center of each Gaussian profile. Blue curves are the sum of the component curves when applicable. Samples were prepared in 1× TBE with 15mM MgCl<sub>2</sub> at a nominal 5 μM. Temperature was increase at 1 °C per minute with absorbance data collected every 0.25 °C (15 seconds) from 60 °C to 98 °C.

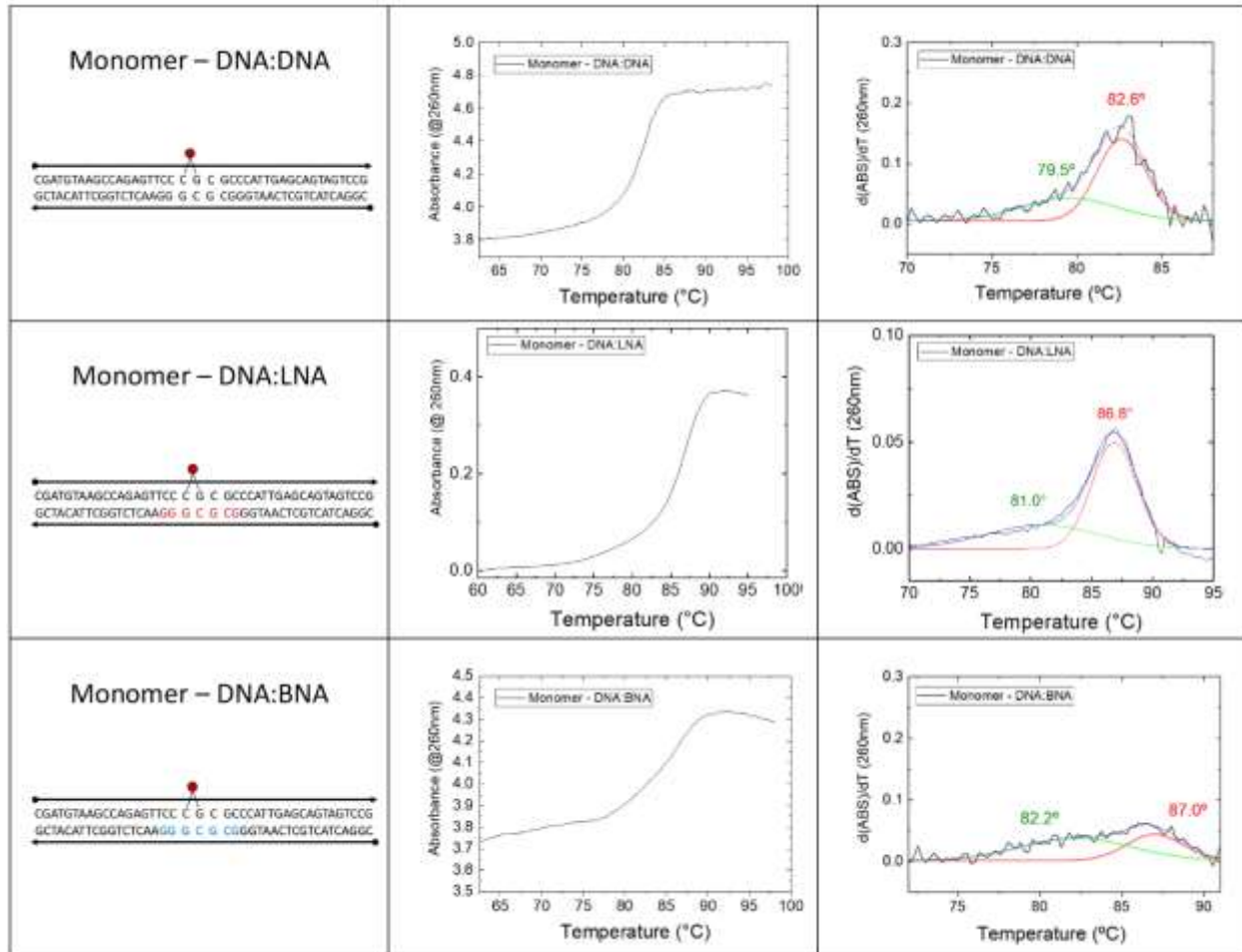


**Figure S2:** Schematics for monomer samples (left) with temperature-dependent absorbance at 260nm (center) and the first derivative with respect to temperature (right). Derivative curves were decomposed into one or more Gaussian profiles using Origin Pro (2019b). Temperatures for pre-melting (green) and main (red) melting transitions were determined by noting the center of each Gaussian profile. Blue curves are the sum of the component curves when applicable. Samples were prepared in 1× TBE with 15mM MgCl<sub>2</sub> at a nominal 5 μM. Temperature was increase at 1 °C per minute with absorbance data collected every 0.25 °C (15 seconds) from 60 °C to 98 °C.

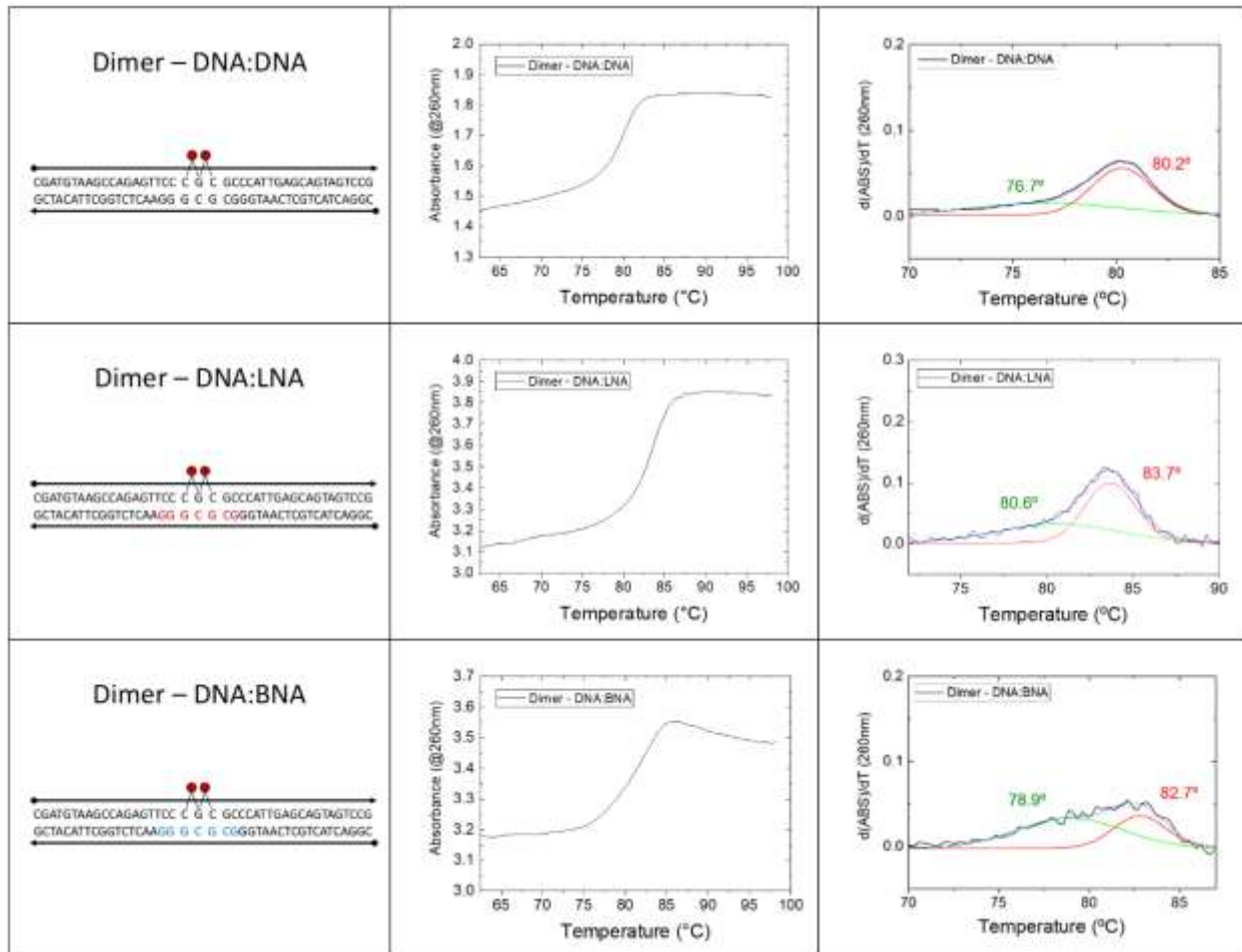


**Figure S3:** Schematics for dimer samples (left) with temperature-dependent absorbance at 260nm (center) and the first derivative with respect to temperature (right). Derivative curves were decomposed into one or more Gaussian profiles using Origin Pro (2019b). Temperatures for pre-melting (green) and main (red) melting transitions were determined by noting the center of each Gaussian profile. Blue curves are the sum of the component curves when applicable. Samples were prepared in 1× TBE with 15mM MgCl<sub>2</sub> at a nominal 5 μM. Temperature was increase at 1 °C per minute with absorbance data collected every 0.25 °C (15 seconds) from 60 °C to 98 °C.

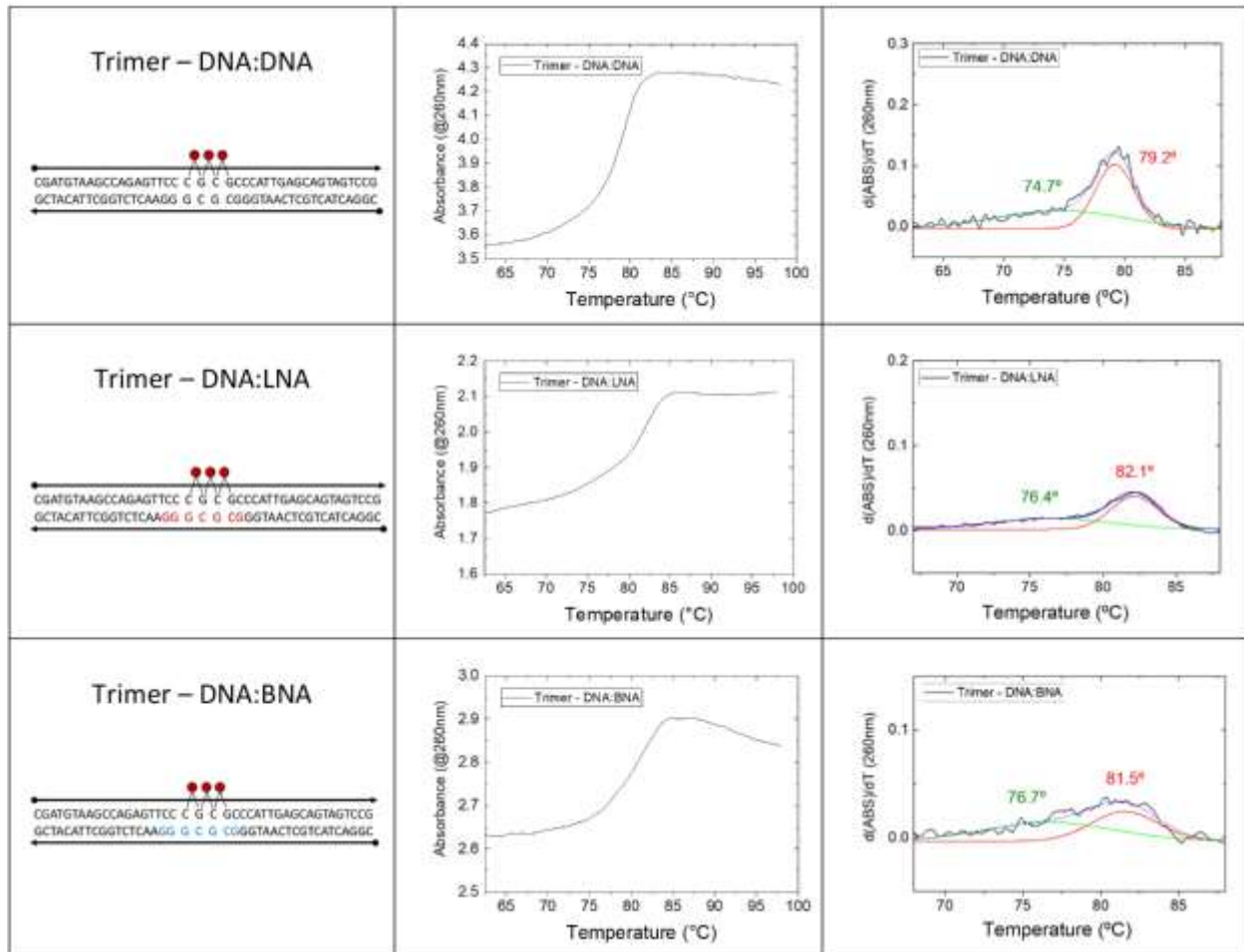


**Figure S4:** Schematics for trimer samples (left) with temperature-dependent absorbance at 260nm (center) and the first derivative with respect to temperature (right). Derivative curves were decomposed into one or more Gaussian profiles using Origin Pro (2019b). Temperatures for pre-melting (green) and main (red) melting transitions were determined by noting the center of each Gaussian profile. Blue curves are the sum of the component curves when applicable. Samples were prepared in 1× TBE with 15mM MgCl<sub>2</sub> at a nominal 5 μM. Temperature was increase at 1 °C per minute with absorbance data collected every 0.25 °C (15 seconds) from 60 °C to 98 °C.

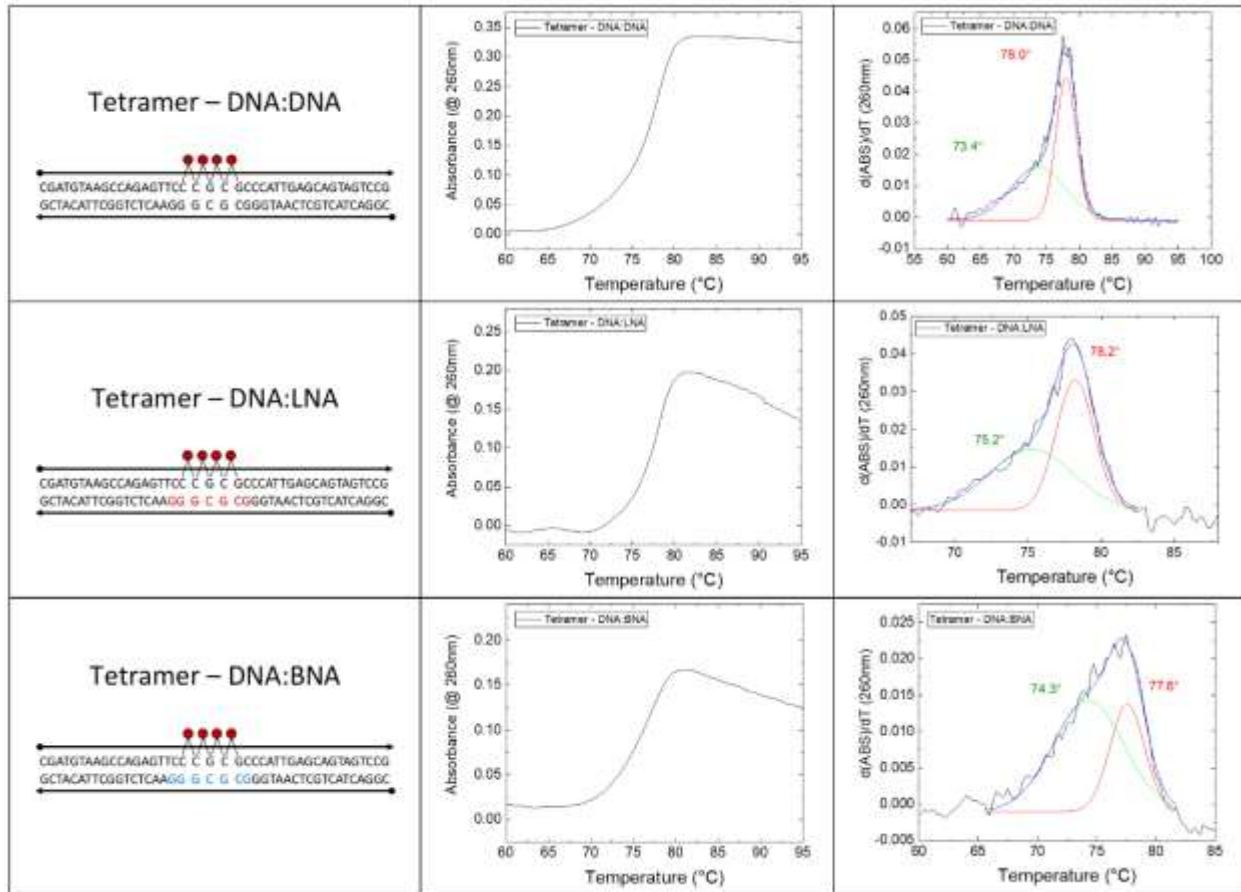


**Figure S5:** Schematics for tetramer samples (left) with temperature-dependent absorbance at 260nm (center) and the first derivative with respect to temperature (right). Derivative curves were decomposed into one or more Gaussian profiles using Origin Pro (2019b). Temperatures for pre-melting (green) and main (red) melting transitions were determined by noting the center of each Gaussian profile. Blue curves are the sum of the component curves when applicable. Samples were prepared in 1× TBE with 15mM MgCl<sub>2</sub> at a nominal 5 μM. Temperature was increase at 1 ° C per minute with absorbance data collected every 0.25 ° C (15 seconds) from 60 ° C to 98 ° C.

**Table S1:** Summary of melting transitions shown in **Figures S1-S5**.

		Main transition (°C)	“Pre-melting” transition (°C)
Unmodified	DNA:DNA	82.4	N/A
	DNA:LNA	90.9	N/A
	DNA:BNA	89.5	N/A
Monomers	DNA:DNA	82.6	79.5
	DNA:LNA	86.8	81.0
	DNA:BNA	87.0	82.2
Dimers	DNA:DNA	80.2	76.7
	DNA:LNA	83.7	80.6
	DNA:BNA	82.7	78.9
Trimers	DNA:DNA	79.2	74.7
	DNA:LNA	82.1	76.4
	DNA:BNA	81.5	76.7
Tetramers	DNA:DNA	78.0	73.8
	DNA:LNA	78.2	75.2
	DNA:BNA	77.6	74.3



Additional experiments were carried out to evaluate hysteresis as the number of included chromophores was increased. A select set of samples was prepared at 1  $\mu\text{M}$  in 1 $\times$  TBE, 15 mM  $\text{MgCl}_2$ . Melting data were collected as described above and included a ramp down to room temperature (annealing) at the same rate, while continuing to monitor absorbance at 260 nm. The same fitting procedure was applied to determine the melting temperatures for both major and minor transitions for melting and annealing (Figures S6-S12). A summary plot of the main transitions is shown in Figure S13.

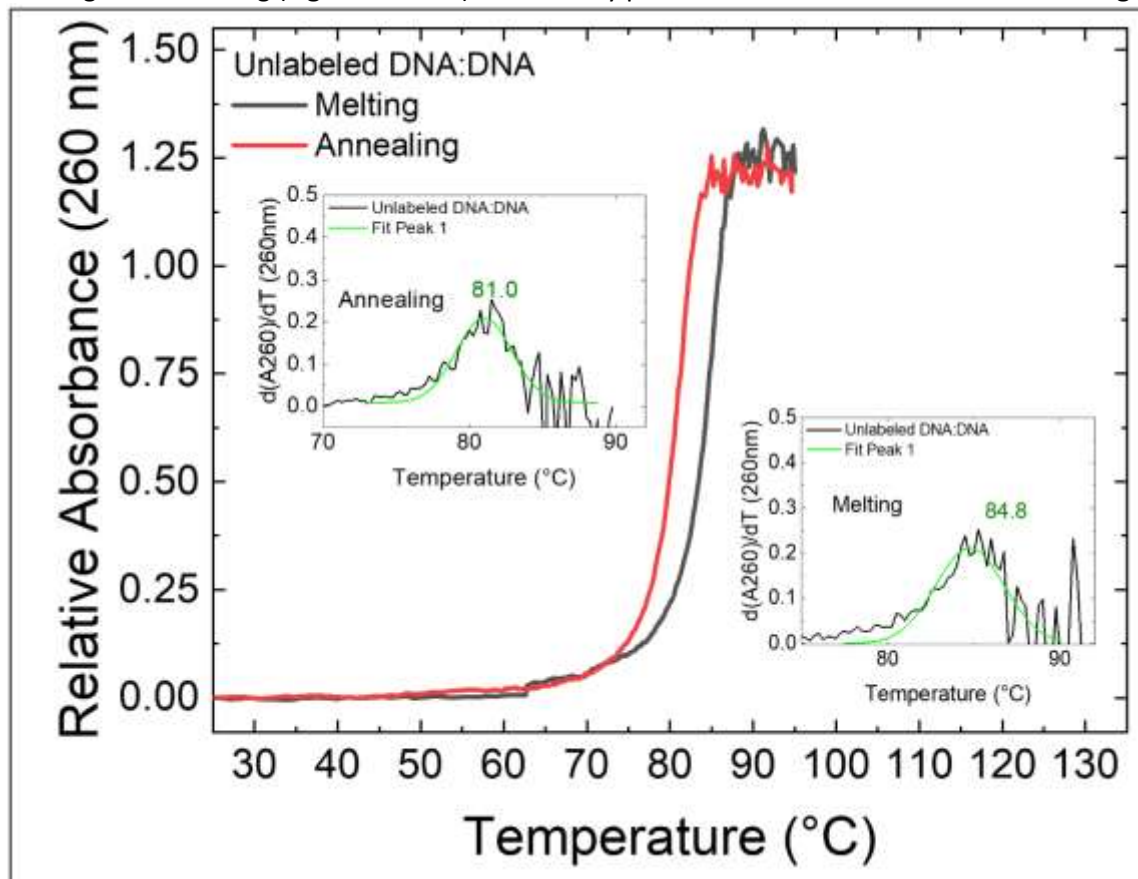


**Figure S6:** Melting (**black**) and annealing (**red**) curves of the unlabeled construct on the DNA:DNA scaffold variant recorded at the sample concentration (1  $\mu\text{M}$  in 1 $\times$  TBE, 15mM  $\text{MgCl}_2$ ; absorbance at 260 nm monitored as temperature increased from 25 °C to 95 °C and back to 25 °C at 1 °C/min). Insets show the derivative of melting and annealing curves with respect to temperature (**black** traces). The melting transition was found by fitting the derivative data with a Gaussian curve (**green**).

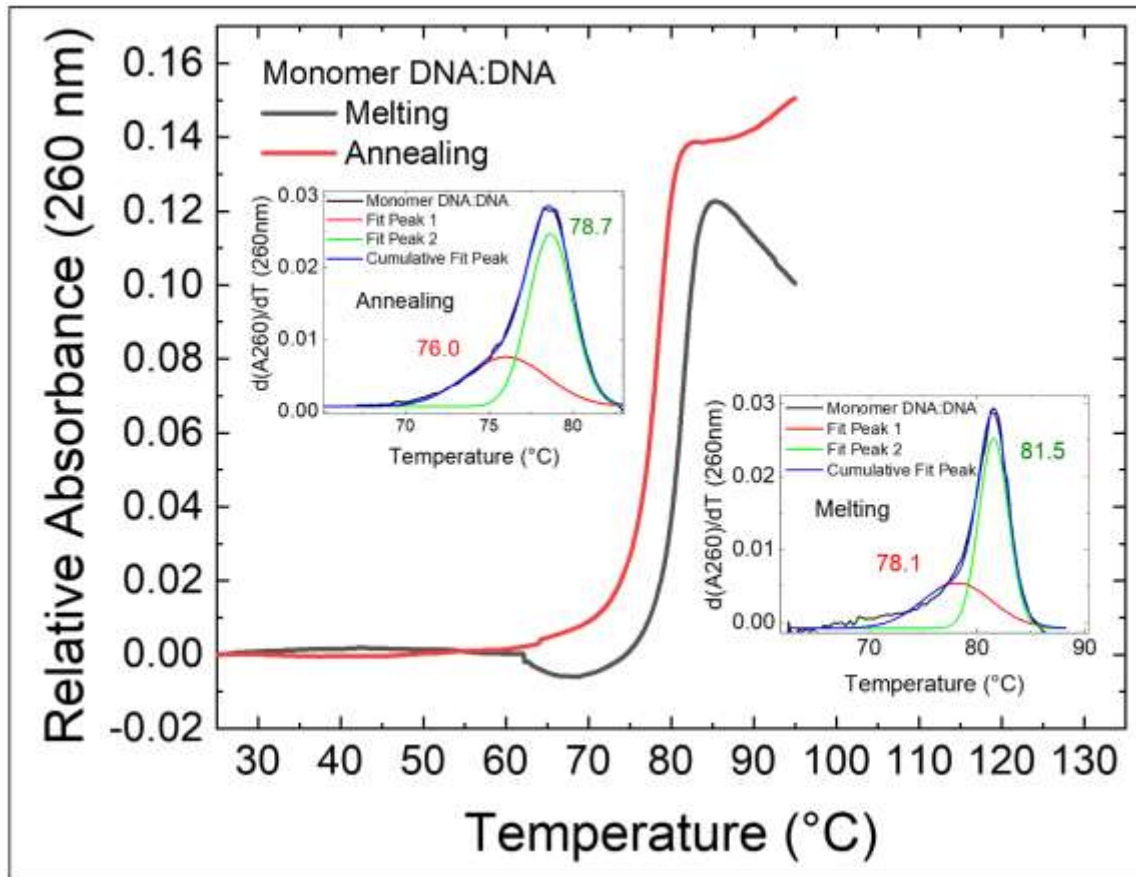


**Figure S7:** Melting (**black**) and annealing (**red**) curves of the monomer construct on the DNA:DNA scaffold variant recorded at the sample concentration (1  $\mu$ M in 1 $\times$  TBE, 15mM MgCl<sub>2</sub>; absorbance at 260 nm monitored as temperature increased from 25 °C to 95 °C and back to 25 °C at 1 °C/min). Insets show the derivative of melting and annealing curves with respect to temperature (**black** traces). Gaussian peaks representing minor transitions (**red**) and major transitions (**green**) sum to form the blue traces.

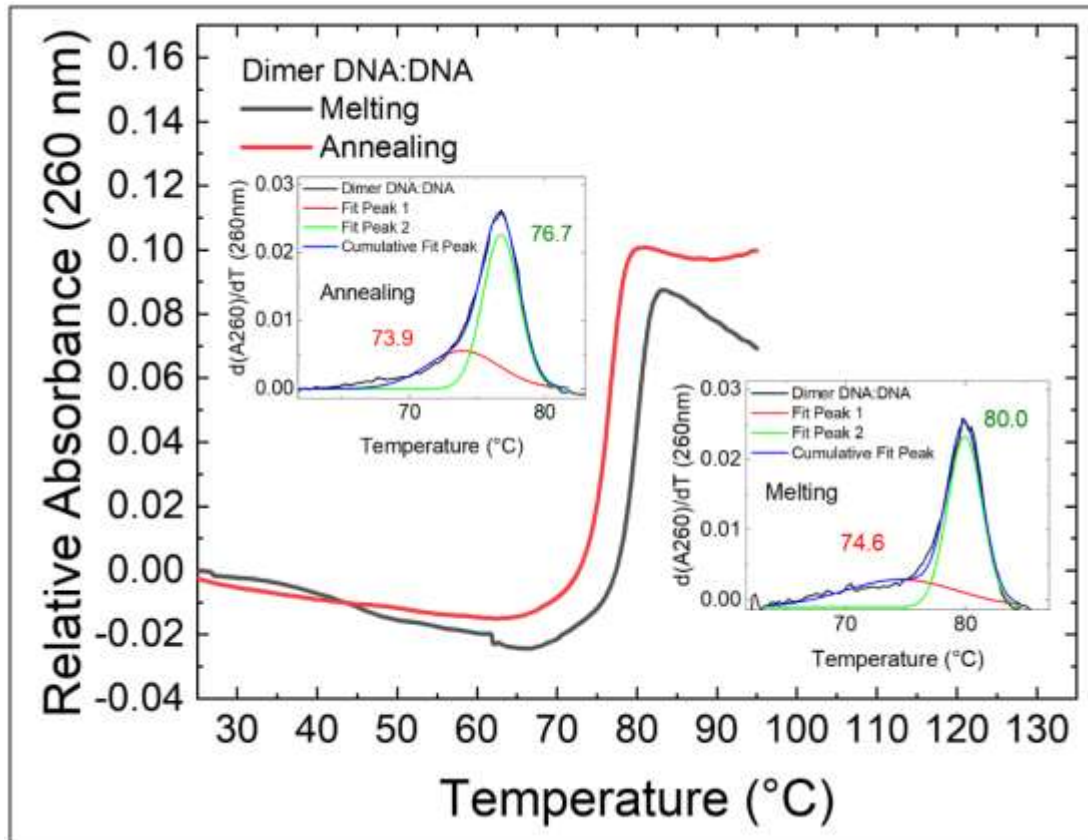


**Figure S8:** Melting (**black**) and annealing (**red**) curves of the dimer construct on the DNA:DNA scaffold variant recorded at the sample concentration (1  $\mu$ M in 1 $\times$  TBE, 15mM MgCl<sub>2</sub>; absorbance at 260 nm monitored as temperature increased from 25 °C to 95 °C and back to 25 °C at 1 °C/min). Insets show the derivative of melting and annealing curves with respect to temperature (**black** traces). Gaussian peaks representing minor transitions (**red**) and major transitions (**green**) sum to form the blue traces.

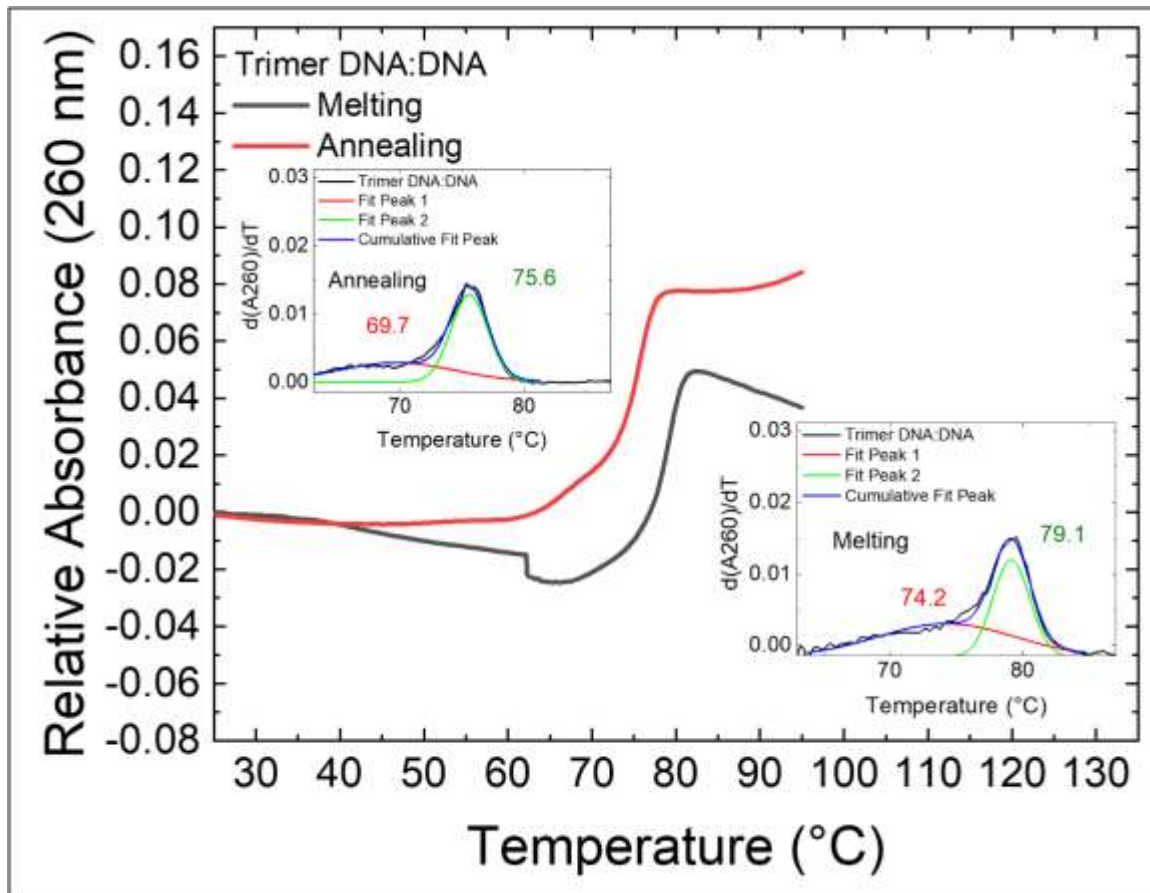


**Figure S9:** Melting (**black**) and annealing (**red**) curves of the trimer construct on the DNA:DNA scaffold recorded at the sample concentration (1  $\mu$ M in 1 $\times$  TBE, 15mM  $MgCl_2$ ; absorbance at 260 nm monitored as temperature increased from 25  $^{\circ}C$  to 95  $^{\circ}C$  and back to 25  $^{\circ}C$  at 1  $^{\circ}C/min$ ). Insets show the derivative of melting and annealing curves with respect to temperature (**black** traces). Gaussian peaks representing minor transitions (**red**) and major transitions (**green**) sum to form the blue traces.

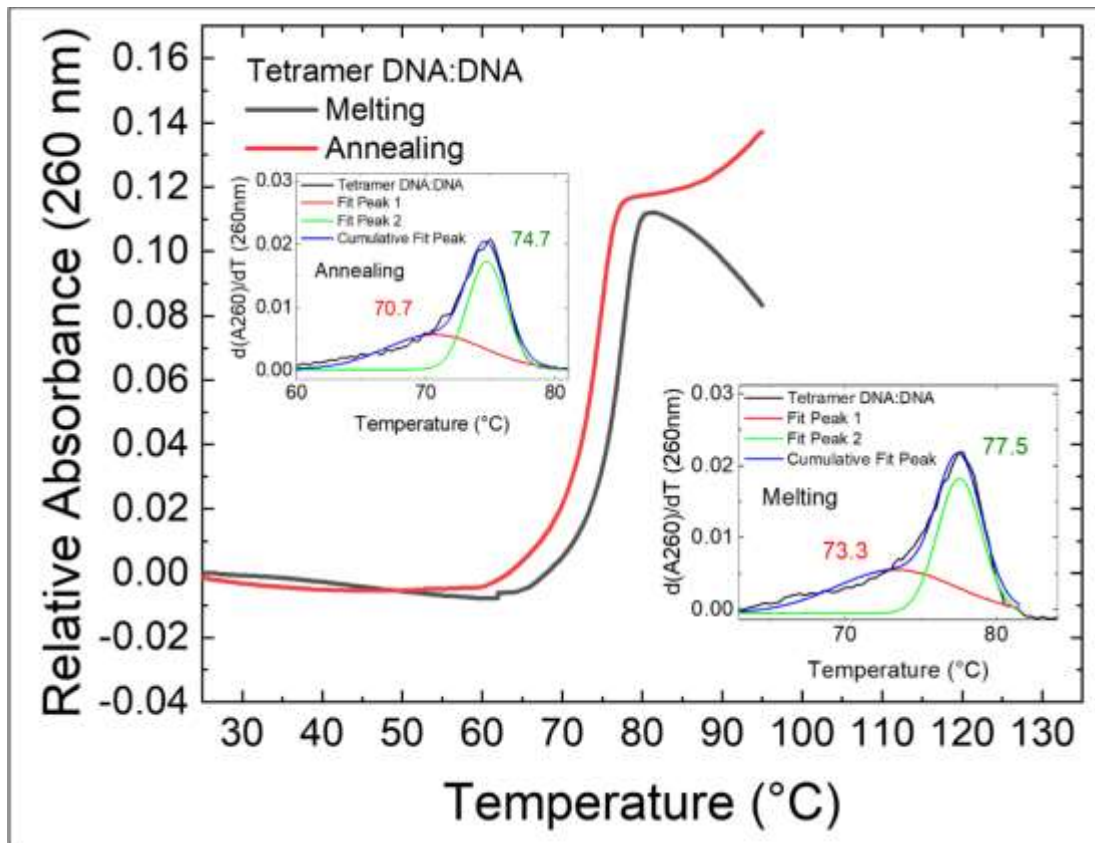


**Figure S10:** Melting (**black**) and annealing (**red**) curves of the tetramer construct on the DNA:DNA scaffold variant recorded at the sample concentration (1  $\mu$ M in 1 $\times$  TBE, 15mM MgCl<sub>2</sub>; absorbance at 260 nm monitored as temperature increased from 25 °C to 95 °C and back to 25 °C at 1 °C/min). Insets show the derivative of melting and annealing curves with respect to temperature (**black** traces). Gaussian peaks representing minor transitions (**red**) and major transitions (**green**) sum to form the blue traces.

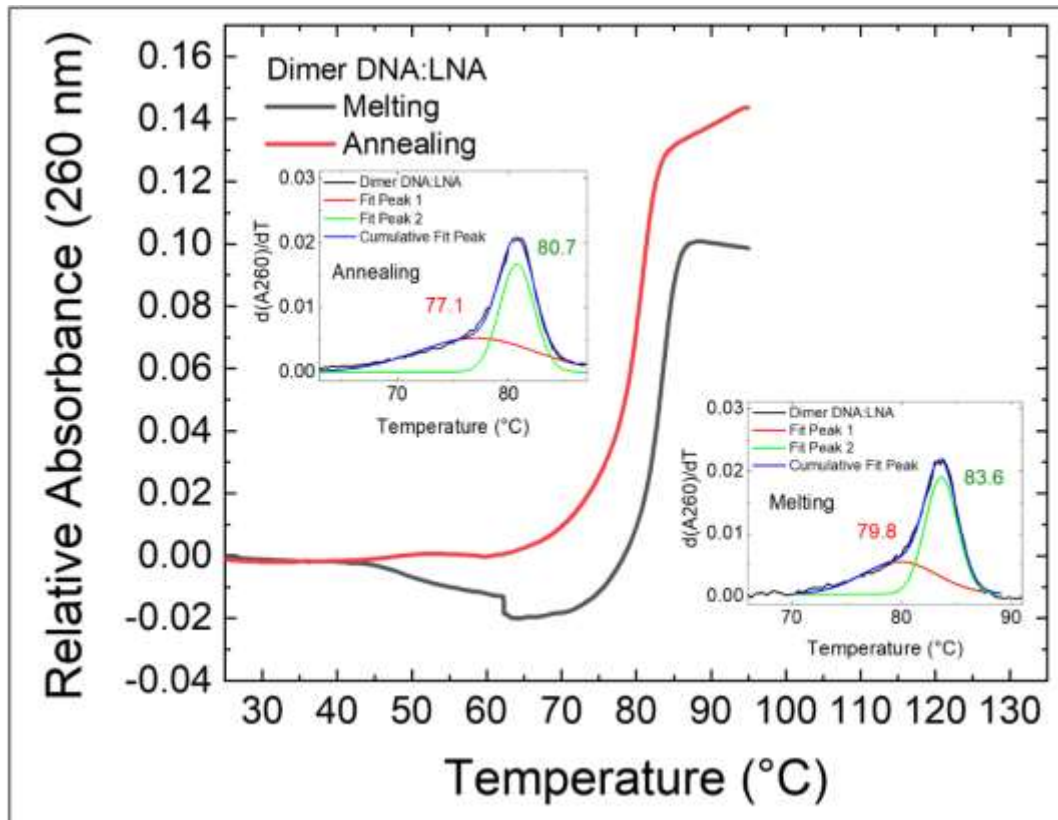


**Figure S11:** Melting (**black**) and annealing (**red**) curves of the dimer construct on the DNA:LNA scaffold recorded at the sample concentration ( $1 \mu\text{M}$  in  $1\times$  TBE,  $15\text{mM}$   $\text{MgCl}_2$ ; absorbance at 260 nm monitored as temperature increased from  $25^\circ\text{C}$  to  $95^\circ\text{C}$  and back to  $25^\circ\text{C}$  at  $1^\circ\text{C}/\text{min}$ ). Insets show the derivative of melting and annealing curves with respect to temperature (**black** traces). Gaussian peaks representing minor transitions (**red**) and major transitions (**green**) sum to form the blue traces.

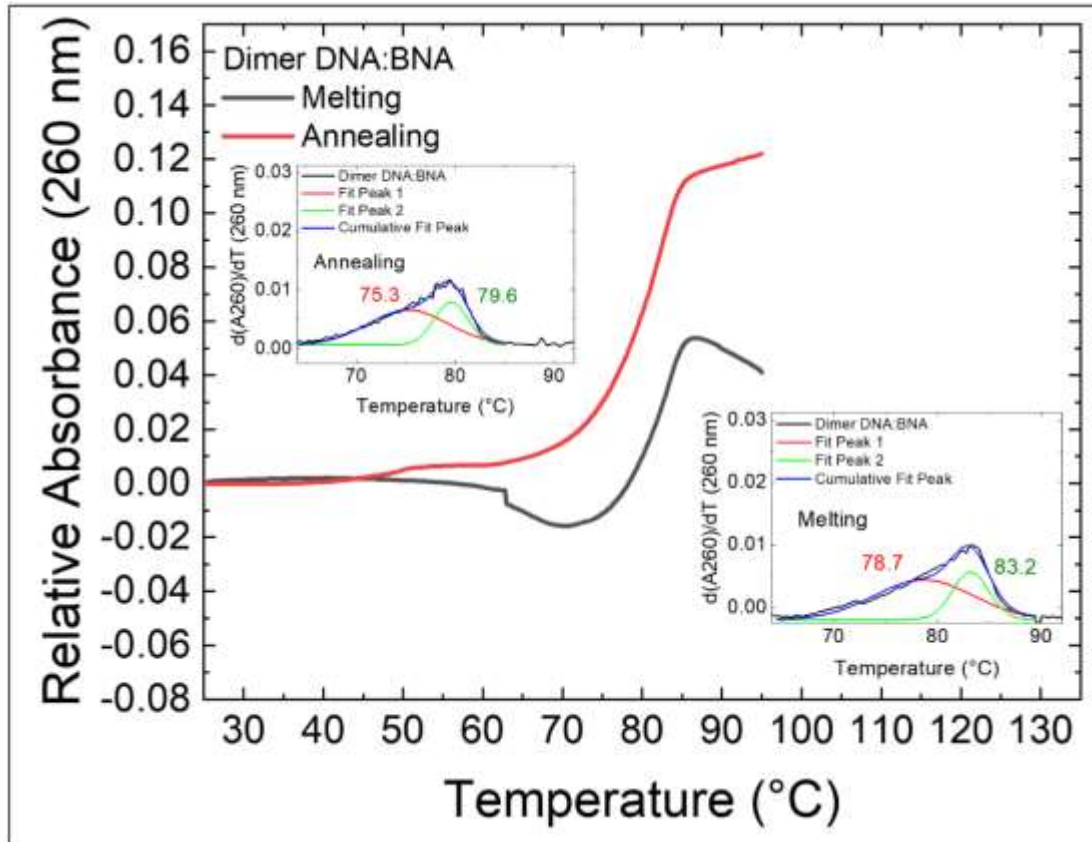


**Figure S12:** Melting (**black**) and annealing (**red**) curves of the dimer construct on the DNA:BNA scaffold variant recorded at the sample concentration (1  $\mu$ M in 1 $\times$  TBE, 15mM MgCl<sub>2</sub>; absorbance at 260 nm monitored as temperature increased from 25  $^{\circ}$ C to 95  $^{\circ}$ C and back to 25  $^{\circ}$ C at 1  $^{\circ}$ C/min). Insets show the derivative of melting and annealing curves with respect to temperature (**black** traces). Gaussian peaks representing minor transitions (**red**) and major transitions (**green**) sum to form the blue traces.

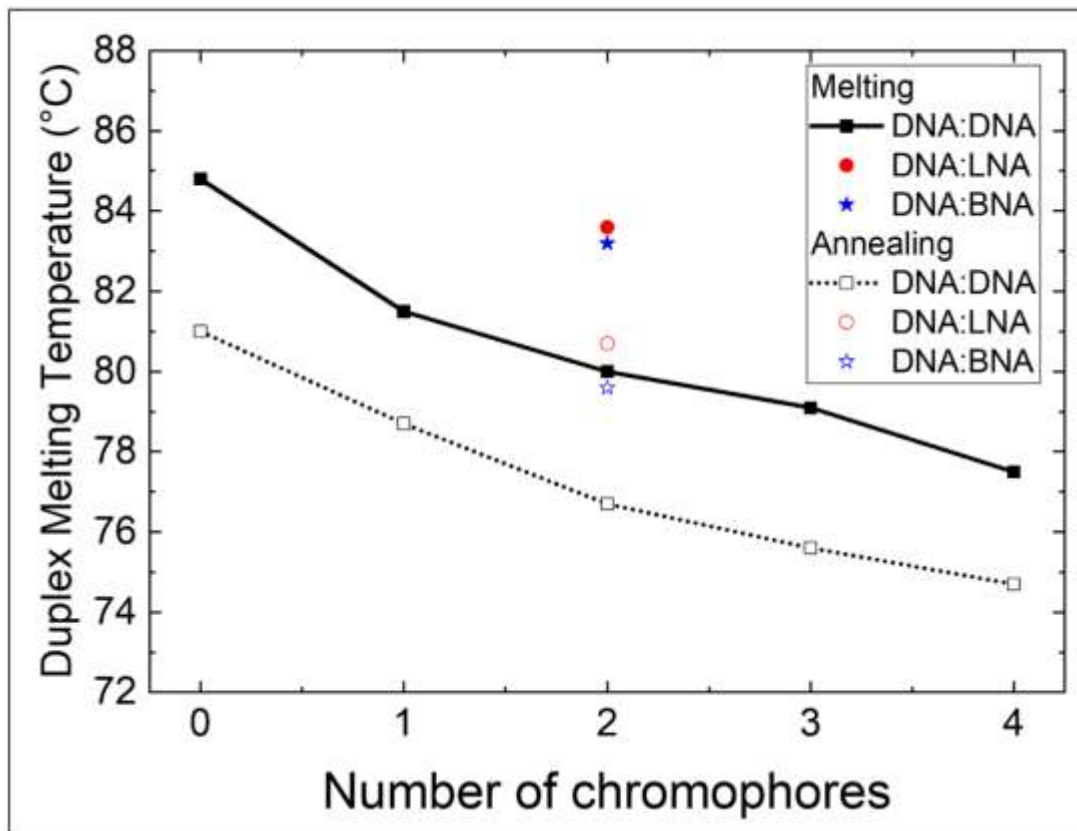


**Figure S13:** Summary of hysteresis results for the main melting transitions shown in **Figures S6-S12**. The solid black trace and solid symbols indicate temperatures derived from an increasing temperature ramp, whereas dotted lines and hollow symbols indicate temperatures derived from a decreasing temperature ramp.

Our results showed that the duplex samples consistently hybridized at a lower temperature during annealing than observed during melting. Using the DNA:DNA template, we observe a consistent shift in peak position in the derived melting transition temperatures of approximately 3 °C that did not change as the number of chromophores increases. The dimer constructs on the DNA:LNA and DNA:BNA templates showed a similar shift in temperatures. We would note that the DNA:BNA dimer melting profile was the least-defined of the set, consistent with melting results for other samples in this study. The derivative curves for the DNA:BNA scaffold variants seemed to suggest a continuous transition rather than distinct melting events.

Important to note for this study, although exact melting temperatures will tend to vary with number of base pairs, sequence, scaffold design, and experimental conditions, we observed the same trends in the melting data for both ramp directions: 1) Melting data suggested that each additional chromophore decreased the temperature of the main melting transition. 2) We observed evidence of multiple melting transitions in both ramp directions. 3) Adding LNA or BNA will increase the melting transition temperature for templates with small aggregates (e.g., dimers).



## S12: Polyacrylamide Gel Electrophoresis (PAGE)

**Figures S14- 216** show full images of 10% PAGE gels shown in the main text. Samples were prepared to a nominal  $5\mu\text{M}$  in  $1\times$  TBE with  $15\text{mM}$   $\text{MgCl}_2$ . Samples were annealed at  $98\text{ }^\circ\text{C}$  for 15 minutes and cooled at  $0.4\text{ }^\circ\text{C}/\text{min}$  to  $25\text{ }^\circ\text{C}$ . Gels were prepared with  $1\times$  TBE in the acrylamide gel without added  $\text{MgCl}_2$ . The running buffer was  $1\times$  TBE with  $15\text{mM}$  added  $\text{MgCl}_2$  (same buffer as sample solutions). Wells in **Figures S14** and **S15** were filled with  $25\text{ }\mu\text{L}$  of sample solution and  $5\text{ }\mu\text{L}$  loading buffer. Gels in **Figure S16** were filled with  $20\text{ }\mu\text{L}$  of sample,  $3\text{ }\mu\text{L}$  of loading buffer, and  $2\text{ }\mu\text{L}$  of Sybr-Au intercalating dye for visualization. Gels were held at  $15\text{ }^\circ\text{C}$  with a water circulator while  $150\text{V}$  was applied across the gel terminals for 90 minutes. Current averaged  $\sim 50\text{ mA}$  during the electrophoresis. Gels were imaged using Epi-UV illumination on a phosphor plate.

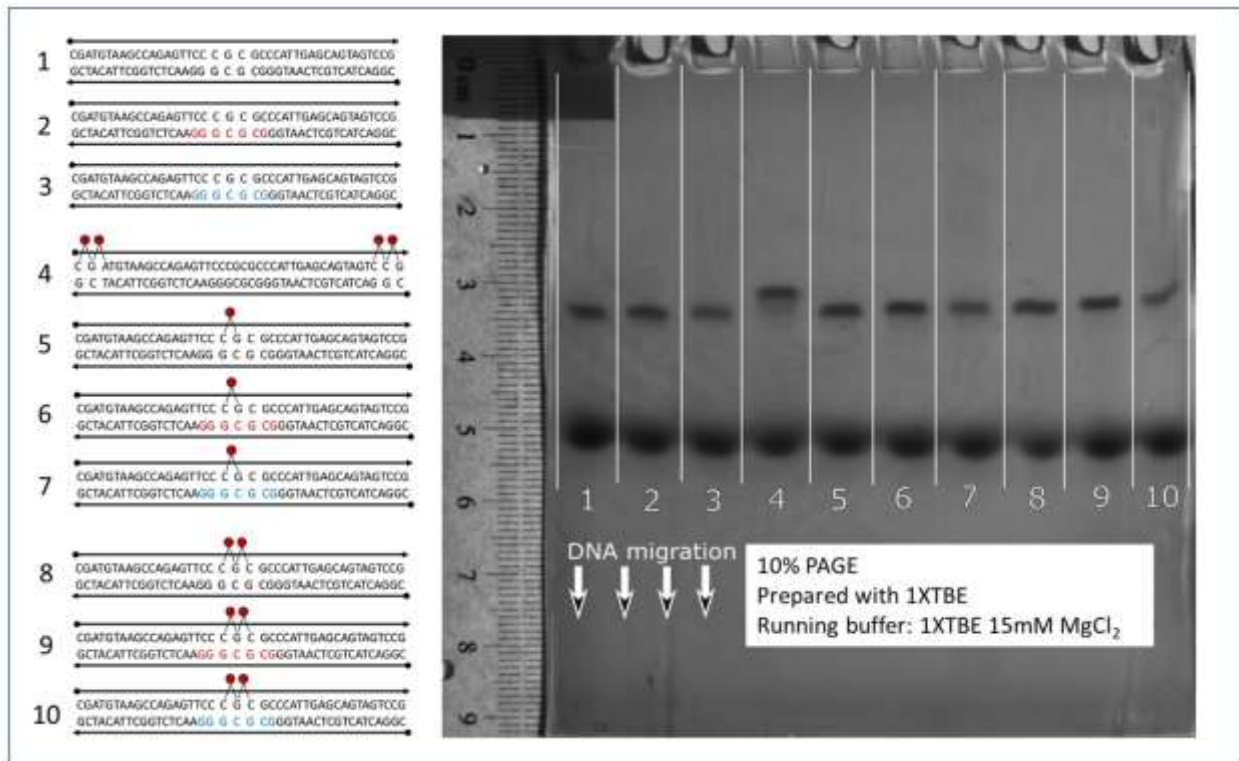


**Figure S14:** 10% PAGE gel image (1.5 mm; casted in  $1\times$  TBE) after samples were annealed. Each numbered schematic in the left column corresponds to a numbered lane in the gel. This gel compares monomers and dimers to unlabeled duplexes. Lane 4 contains a tetramer for comparison. Lanes 1–4 appear in the main text (**Figure 3a**). Samples and gels were prepared as described above.

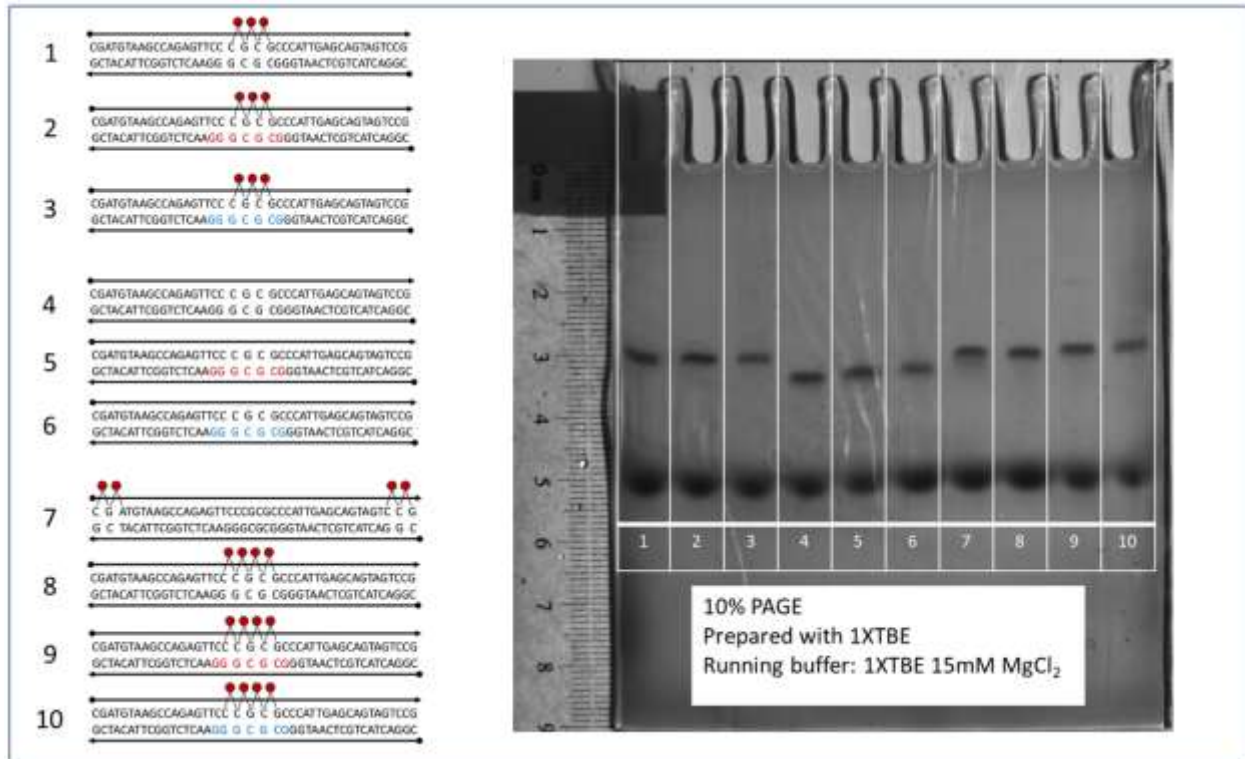


**Figure S15:** PAGE gel image after samples were annealed. Each numbered schematic in the left column corresponds to a numbered lane in the gel. This gel compares trimers and tetramers to unlabeled duplexes. Lanes 7 and 8 appear in the main text (**Figure 3c**). Samples and gels were prepared as described above.

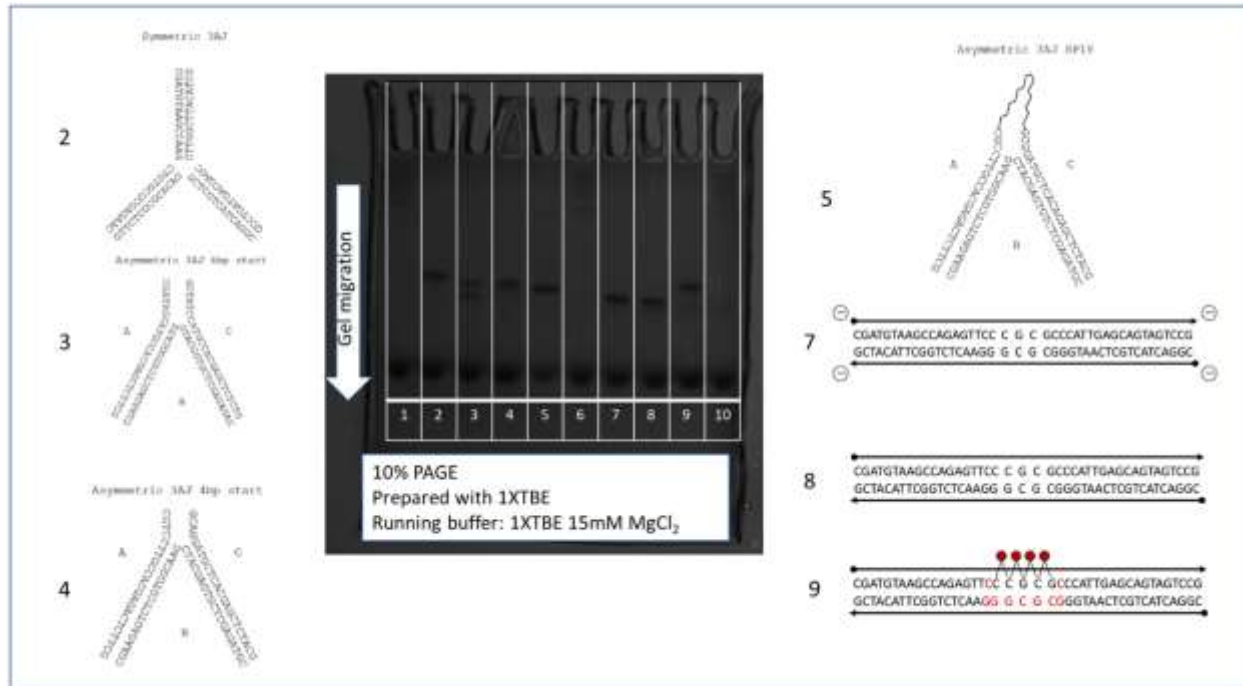


**Figure S16:** PAGE gel image showing a series of structures to compare with an unmodified duplex (lane 8). Lanes 7 (duplex with extra negatively charged groups) and 8 appear in the main text (**Figure 3a**). Lane 3 contained a symmetric three-arm junction. Lane 4 contained a three-arm junction with one short arm (6 bp). Lane 4 contained a similar asymmetric three-arm junction with a 4 bp arm. Lane 5 contained an asymmetric three-arm junction with a 3-bp arm and an 18-atom hexa-ethleneglycol spacer (IDT). Lanes 1, 6, and 10 each contained a low molecular weight DNA ladder that did not provide any relevant information. Samples and gels were prepared as described above.

The purpose of the gel in **Figure S16** was to explore the possibility that the helical axis of our duplexes was being “bent” by the attached chromophores and to assess the role of charge in the migration rate. Lanes 2 through 5 were intended to provide insight into the potential bending of the helical axis caused by chromophore inclusion. Although we observed a trend of increased mobility in the gel as the short arm of the three-arm junctions gets shorter, we were unable to any draw strong conclusions relevant to our study from the migration rates of these structures. Lanes 7 through 9 were intended to assess the role of charge in migration rates of a 42 bp duplex. Lane 7 contained a duplex with the equivalent of two additional negative charges compared with the unmodified duplex in lane 8. Instead of increasing the migration rate, we observed a slower migration rate. We infer that the additional bulk of the charged groups was a dominant influence in migration relative to the additional charges. The significantly slower migration observed in lane 9 with four attached Cy5 chromophores suggest that the chromophores either 1) disturb the linearity of the helical axis, 2) run slower due to additional positive charges on the Cy5 chromophores, or 3) simply run slower due to the added bulk of the chromophore molecules. The comparison between lanes 7 and 8 in **Figure S16** suggests that charge was not a major factor. Additionally, the comparison between lanes 7 and 8 in **Figure S15** suggests that the chromophores did not cause a significant bend in the helical axis. We thus conclude that the major factor influencing migration rate in the gel was molecular weight, as expected.

### Reduction in Scaffold Heterogeneity by Annealing

To assess the effectiveness of thermal annealing during sample preparation, PAGE gel images were obtained for samples before and after an annealing procedure. **Figures S17** and **S18** show images for gels prepared with the same protocol as the gels in **Figures S14** and **S15**; however, the samples were not annealed after combining the component strands. We concluded that, within the detection limits of the imaging system, the annealing cycle was effective in eliminating unwanted secondary DNA scaffold structures. We assigned the secondary bands to so-called “mobile” Holliday junctions or higher order combinations of DNA strands. These bands are only visible for samples containing attached chromophores, possibly suggesting that inter-chromophore attractive forces can promote formation of unwanted structures in unannealed samples.

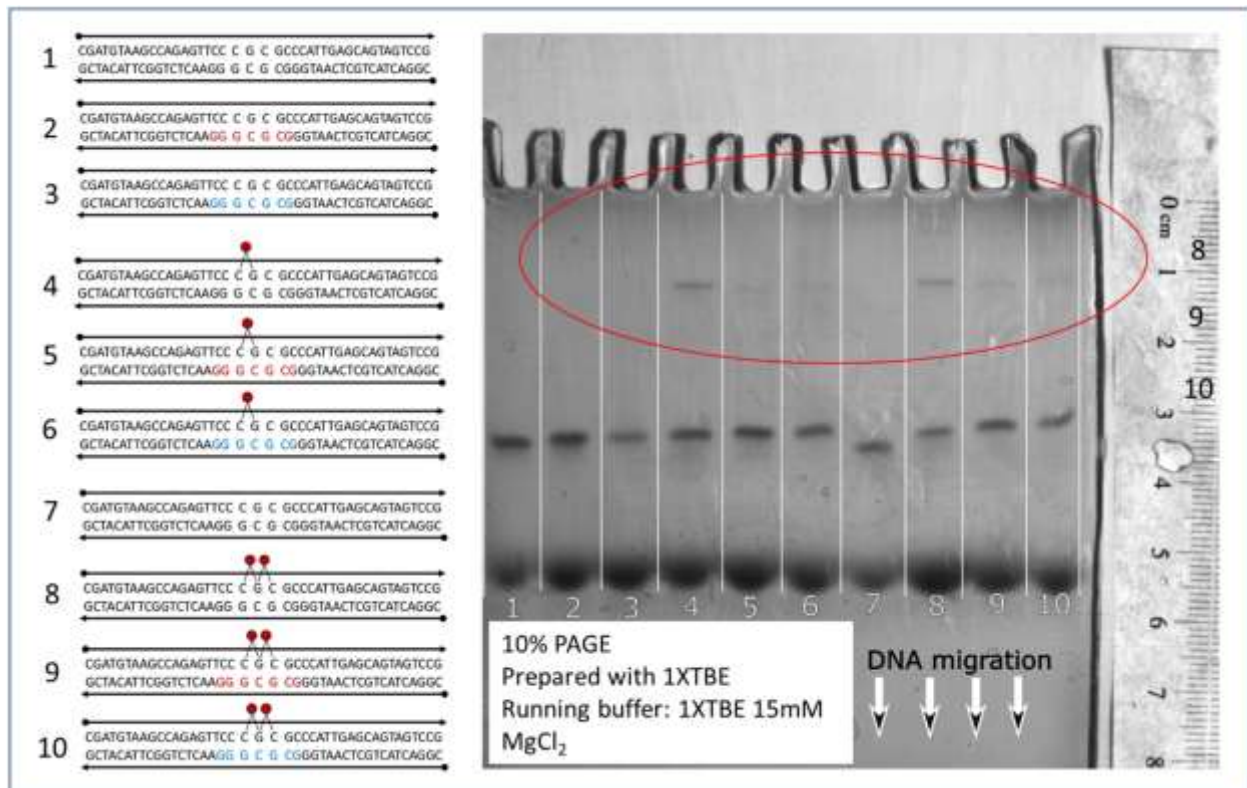


**Figure S17:** PAGE gel image comparing unlabeled, monomer, and dimer samples before annealing. This gel is nearly identical to the gel in **Figure S14**. Unwanted higher order scaffold structures are clearly visible in the gel before annealing, as denoted by the bands encircled in red. This gel was prepared with the same protocol and samples as **Figure S14**, but before the annealing cycle.

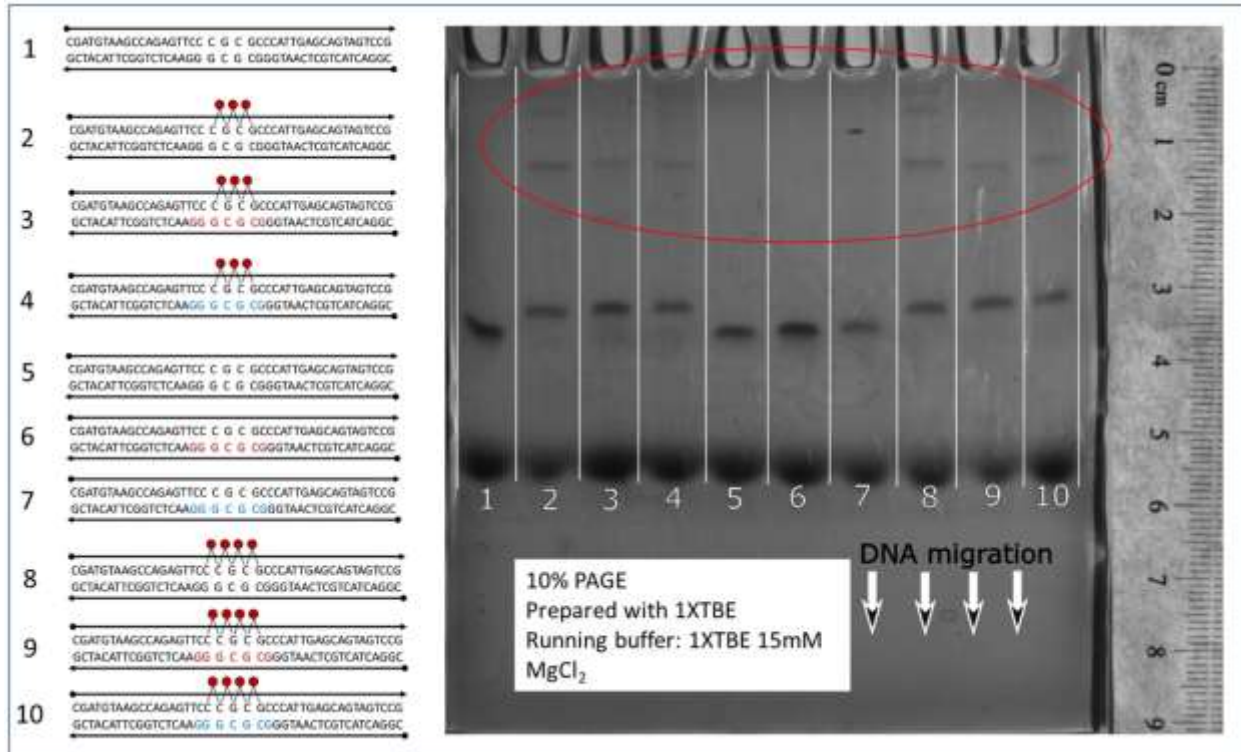


**Figure S18:** PAGE gel image comparing unlabeled samples with trimers and tetramers before annealing. Again, many secondary scaffold structures were present in the gel for samples containing chromophores, as denoted by the bands encircled in red. This gel was prepared with the same protocol and samples as **Figure S15**, but before the annealing cycle.

## S13 Theoretical Modeling

**Summary:** The KRM Model Simulation Tool, based on theory developed by Kühn, Renger, and May (KRM)<sup>1</sup>, was used to simultaneously fit experimental absorbance and circular dichroism (CD) spectra. The KRM Model Simulation Tool utilizes a system Hamiltonian to predict theoretical spectra arising from specific relative orientations of two or more monomer transition dipole moments. The software uses an iterative stochastic gradient search approach guided by goodness of fit parameters (described below) to reproduce experimental spectra. Model outputs encompass the relative TDM positions and orientations along with normalized theoretical spectra and other system parameters.

*System Hamiltonian*

Molecular (Frenkel) exciton behavior is well approximated by a Holstein-like<sup>2</sup> augmented Frenkel Hamiltonian<sup>3-5</sup> of the form:

$$\hat{H} = \hat{H}^{(e)} + \hat{H}^{(v)} \quad (1)$$

where  $\hat{H}^{(e)}$  and  $\hat{H}^{(v)}$  represent the electronic and vibronic components, respectively, of the total Hamiltonian.

The KRM Model Simulation Tool considers the case of single excitations. Terms involving double excitations are omitted, and the electronic part of the Hamiltonian becomes:

$$\hat{H}^{(e)} = \sum_m \varepsilon_m^e \hat{B}_m^\dagger \hat{B}_m + \sum_{m,n}^{m \neq n} J_{m,n} \hat{B}_m^\dagger \hat{B}_n \quad (2)$$

where  $\varepsilon_m^e$  is the monomer transition energy,  $J_{m,n}$  is the exchange energy—or excitonic hopping parameter—associated with transition dipole coupling between chromophores  $m$  and  $n$  from a single exciton, and the operators  $\hat{B}_i^\dagger$  and  $\hat{B}_i$  are exciton creation and annihilation operators, respectively. The monomer transition energy,  $\varepsilon_m^e$ , is determined from the experimental monomer absorbance spectrum and is taken to be the peak position of the 0-0 transition and remains constant throughout the fitting process. In contrast  $J_{m,n}$  is sensitive to relative orientations and inter-chromophore distances, and thus must be calculated for each pair of TDMs for each fitting step. Thus, for a dye aggregate larger than a dimer, a matrix of  $J_{m,n}$ s will be calculated.

The excitonic hopping parameter is often calculated using the point-dipole approximation:

$$J_{m,n} = \frac{1}{4\pi\varepsilon_0\varepsilon_r} \left( \frac{\boldsymbol{\mu}_m \cdot \boldsymbol{\mu}_n}{|\mathbf{R}_{m,n}|^3} - 3 \frac{(\boldsymbol{\mu}_m \cdot \mathbf{R}_{m,n})(\boldsymbol{\mu}_n \cdot \mathbf{R}_{m,n})}{|\mathbf{R}_{m,n}|^5} \right) \quad (3)$$

where  $\mathbf{R}_{m,n}$  is the separation vector between the centers of the TDM vectors described by  $\boldsymbol{\mu}_m$  and  $\boldsymbol{\mu}_n$ . The point-dipole approximation, however, is not strictly valid when intermolecular distances are smaller or on the same order as the size of the dipole moments. Instead, an extended dipole approximation<sup>6</sup> is utilized:

$$J_{m,n} = \frac{\delta_m \delta_n}{4\pi\epsilon_0\epsilon_r} \left( \frac{1}{|\mathbf{r}_n - \mathbf{r}_m|} - \frac{1}{|\mathbf{r}_n - \mathbf{s}_m|} - \frac{1}{|\mathbf{s}_n - \mathbf{r}_m|} + \frac{1}{|\mathbf{s}_n - \mathbf{s}_m|} \right) \quad (4)$$

where  $\delta_m$  and  $\delta_n$  are oscillating point charges (in Coulombs) on chromophores  $m$  and  $n$ ,  $\epsilon_0$  is the permittivity of free space ( $8.85 \times 10^{-12} \frac{A^2 s^4}{m^3 kg}$ ),  $\epsilon_r$  is the relative dielectric constant, and the vectors  $\mathbf{r}_i$  and  $\mathbf{s}_i$  define the locations of + and – charges at the ends of each TDM vector (see **Figure S19**)

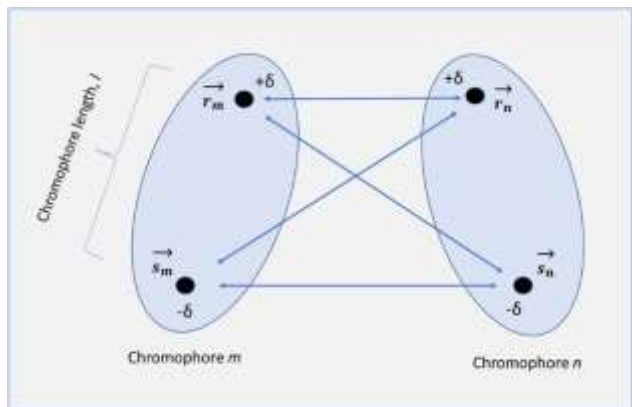


**Figure S19:** Depiction of point charge separation vectors and TDM length,  $l$ , used to calculate  $J_{m,n}$ .

Assuming all chromophores are identical, the transition dipole moment can be written as  $\mu = \delta l$ , where  $l$  is the length of the TDM. Substituting into equation (4) and using  $\epsilon_r = n^2$ , where  $n$  is the index of refraction of the medium, one obtains:

$$J_{m,n} = \frac{1}{l^2} \frac{\mu^2}{4\pi\epsilon_0 n^2} \left( \frac{1}{|\mathbf{r}_n - \mathbf{r}_m|} - \frac{1}{|\mathbf{r}_n - \mathbf{s}_m|} - \frac{1}{|\mathbf{s}_n - \mathbf{r}_m|} + \frac{1}{|\mathbf{s}_n - \mathbf{s}_m|} \right) \quad (5)$$

The magnitude of the monomer transition dipole moment,  $\mu$ , is calculated from the experimental monomer spectrum using:

$$\mu \text{ (debye)} = 9.58 \times 10^{-2} \left( \frac{(2n^2 + 1)^2}{9n^3} \int \frac{\epsilon(\nu)}{\nu} d\nu \right)^{\frac{1}{2}} \quad (6)$$

where  $n$  is the refractive index,  $\epsilon$  is the molar extinction coefficient (in  $M^{-1}cm^{-1}$ ), and  $\nu$  is the wavenumber in  $cm^{-1}$ . Note: 1 debye =  $3.33564 \times 10^{30} C \cdot m$ .

The magnitude of  $\mu$  is assumed to be equal for all chromophores; therefore, it is convenient to write:

$$J_{m,n} = \frac{J_0}{l^2} \left( \frac{1}{|\mathbf{r}_n - \mathbf{r}_m|} - \frac{1}{|\mathbf{r}_n - \mathbf{s}_m|} - \frac{1}{|\mathbf{s}_n - \mathbf{r}_m|} + \frac{1}{|\mathbf{s}_n - \mathbf{s}_m|} \right) \quad (7)$$

where the *characteristic excitonic hopping parameter* has been defined as:

$$J_0 \equiv \frac{\mu^2}{4\pi\epsilon_0 n^2} \quad (8).$$

Using  $n = 1.33$  as the index of refraction and converting to  $meV \cdot nm^3$ ,  $J_0$  is calculated for chromophore pairs on each scaffold type and reported in the tables below.

In addition to the electronic components described above, the KRM Model Simulation Tool considers coupling with up to two vibrational quanta. The exciton-vibron coupling Hamiltonian can be written as:

$$\hat{H}^{(v)} = \sum_m \sum_\alpha \epsilon_m^v \hat{A}_{m,\alpha}^\dagger \hat{A}_{m,\alpha} + \sum_m \sum_\alpha D_{m,\alpha} \hat{B}_m^\dagger \hat{B}_m (\hat{A}_{m,\alpha}^\dagger + \hat{A}_{m,\alpha}) \quad (9)$$

where  $\epsilon_m^v$  is the energy spacing between vibrational levels,  $D_{m,\alpha}$  is related to the displacement of the harmonic oscillator potential of the excited state from the electronic ground state minimum (see **Figure S20** and **Table S2**), and  $\hat{A}_{m,\alpha}^\dagger$  and  $\hat{A}_{m,\alpha}$  are the vibron creation and annihilation operators for chromophore  $m$  and vibrational mode  $\alpha$ . Vibrational energy spacing and displacement are determined using experimental data from the relevant monomer.

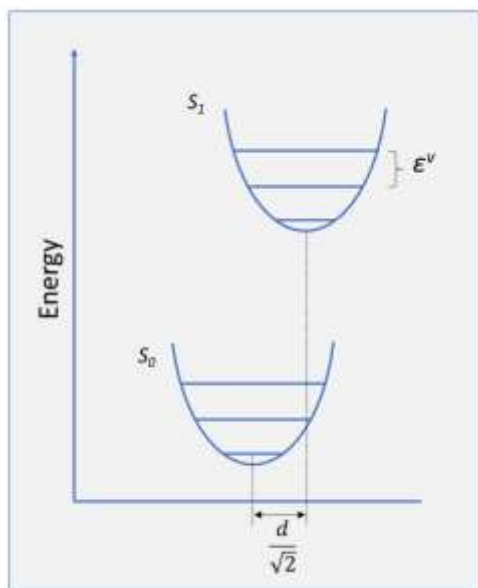


**Figure S20:** Depiction of harmonic oscillator potential surfaces representing the ground state and excited state with vibrational energy level spacing of  $\epsilon^v$  and displacement of potential energy surfaces given by the dimensionless factor  $\frac{d}{\sqrt{2}}$ . The displacement is related to the Huang-Rhys factor (see **Table S2**).



### System Parameters

Inputs and key parameters needed to run the KRM Model Simulation Tool are described in the following table.

**Table S3:** Key parameters estimated from experimental monomer absorbance data.

Parameter	Description
Energy of a vibron, $\varepsilon_m^v$	Energy spacing between vibrational states ( <b>Figure S20</b> )
Displacement, $d$	Dimensionless parameter (specifically, units are a ratio of energy versus energy) related to the displacement of the excited harmonic oscillator potential from the ground-state potential (See <b>Figure S20</b> ). Related to the Huang-Rhys factor as described below.
Energy loss parameter, $\Gamma$	Half-width-at-half-max (HWHM) of 0-0 monomer transition.
Characteristic exciton hopping parameter, $J_0$	Constant pre-factor for calculation of exciton hopping parameter, $J_{m,n}$ , described in detail in the previous section.
Huang-Rhys factor, $\left(\frac{D_{m,\alpha}}{\varepsilon_m^v}\right)^2$	Parameter describing exciton coupling to vibronic modes. $\text{Huang - Rhys factor} = \left(\frac{D_{m,\alpha}}{\varepsilon_m^v}\right)^2 = \frac{d^2}{2}$ where $d$ is the dimensionless displacement described above.
Transition dipole moment, $\mu$	Transition dipole moment in debye units (see previous section).

In addition to the above parameters, the KRM Model Simulation Tool takes in experimental absorbance ( $A_{ex}$ ) and CD spectra ( $A_{ex}^{CD}$ ) for a given aggregate for comparison with theoretical spectra. Also included is a user-selected value for an energy offset from the monomer transition,  $Eof$ , the meaning of which can be inferred from **Figure S21**.

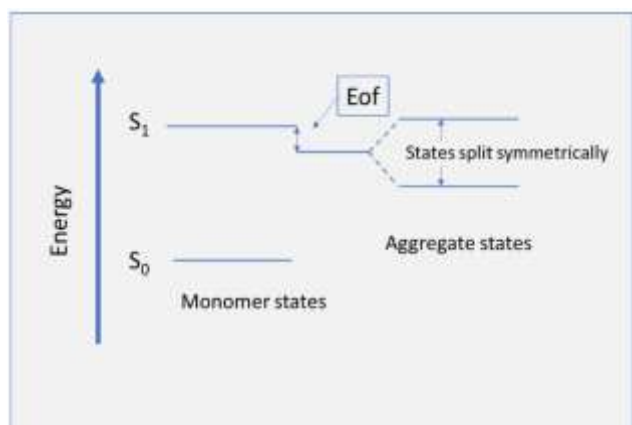


**Figure S21:** Depiction of the effect of the  $Eof$  parameter: energy offset from the monomer excited state. Note: In principle,  $Eof$  can be positive or negative.

### Computing Theoretical Spectra from Initial Orientation

The transition dipole moments (one for each chromophore) are assigned to initial positions (in Cartesian coordinates) defining the center point of each TDM and extending along an orientation vector (defined by polar and azimuthal angles) to span a length  $l$  (estimated from a molecular model of the chromophore).

The coordinates, angles, and TDM length are used to determine vectors  $\mathbf{r}_i$  and  $\mathbf{s}_i$  to calculate  $J_{m,n}$  for each pair of chromophores. The resulting  $J_{m,n}$  and other key parameters are used to populate the system Hamiltonian that is subsequently diagonalized to obtain energies  $E_i$  and to find transition amplitudes for linear absorbance ( $\gamma_i$ ) and circular dichroism ( $\gamma_i^{CD}$ ).

A theoretical absorbance spectrum as a function of energy is assembled by convolving each eigenenergy with a Gaussian line shape according to:

$$A_{th}(E) = \sum_i \frac{\gamma_i}{\sqrt{2\pi}\Gamma^2} e^{-\left(\frac{E-E_i}{2\Gamma^2}\right)^2} \quad (10)$$

A theoretical CD spectrum is similarly determined using:

$$A_{th}^{CD}(E) = \sum_i \frac{\gamma_i^{CD}}{\sqrt{2\pi}\Gamma^2} e^{-\left(\frac{E-E_i}{2\Gamma^2}\right)^2} \quad (11)$$

### Stochastic Gradient Search

To facilitate an efficient search and to evaluate the goodness of fit to experimental data, each set of spectra is given a fitness score (described below). The fitness score is recorded for comparison with later iterations. At each iteration, a TDM position or orientation parameter is randomly selected and changed by a small amount. After each change, a new theoretical spectrum is computed and given a fitness score that is compared with the previous iteration. The program selects the better (lower) fitness score, retains the corresponding orientation information, and moves on to the next iteration. Upon completion, the program outputs results derived from the best observed match between experimental and theoretical spectra. Note: In this study, geometries in which the closest approach for any two TDMs is less than 3.4 angstrom are rejected because the KRM Model Simulation Tool does not currently account for potential orbital overlap that may occur at these smaller separations and require a more extensive treatment.

### Goodness of Fit

Goodness of fit is evaluated using a composite fitness function with up to five user-selected terms that compare experimental and model results.

$$Fitness = w_1 * (1 - RR)^2 + w_2 * (1 - OI_{ABS})^2 + w_3 * (1 - OI_{CD})^2 + w_4 * mS_{ABS} + w_5 * mS_{CD} \quad (12)$$

where  $w_1 \rightarrow w_5$  are user selected coefficients to control the weight of each term. Fitness metrics in each term are calculated as follows:

**Table S4:** Table of fitness metrics used to determine agreement between theoretical and experimental absorbance and CD spectra.

Fitness metric	Description	Equation
Ratio-of-Ratios, $RR$	Ratio of experimental and theoretical maximum values. For a perfect fit, this ratio equals 1.	$\frac{A_{th,max}^{CD}}{A_{th,max}} \frac{A_{ex,max}^{CD}}{A_{ex,max}} \quad (13)$
Absorbance overlap integral, $OI_{ABS}$	Overlap of normalized theoretical and experimental absorbance spectra. For a perfect fit, this integral is equal to 1.	$\frac{\sum_j (A_{th}(E_j) * A_{ex}(E_j))}{[\sum_j (A_{th}(E_j))^2 * \sum_j (A_{ex}(E_j))^2]^{1/2}} \quad (14)$
CD overlap integral, $OI_{CD}$	Overlap of normalized theoretical and experimental CD spectra. For a perfect fit, this integral is equal to 1.	$\frac{\sum_j (A_{th}^{CD}(E_j) * A_{ex}^{CD}(E_j))}{[\sum_j (A_{th}^{CD}(E_j))^2 * \sum_j (A_{ex}^{CD}(E_j))^2]^{1/2}} \quad (15)$
Total overlap integral, $OI_{total}$	The average of $OI_{ABS}$ and $OI_{CD}$	$\frac{OI_{ABS} + OI_{CD}}{2} \quad (16)$
Mean square deviation of absorbance spectra, $ms_{ABS}$	The sum of squared differences between theoretical and experimental absorbance spectra. For a perfect fit, this term is equal to zero.	$\sum_j (A_{th}(E_j) - A_{ex}(E_j))^2 \quad (17)$
Mean square deviation of CD spectra, $ms_{CD}$	The sum of squared differences between theoretical and experimental CD spectra at each energy level. For a perfect fit, this term is equal to zero.	$\sum_j (A_{th}^{CD}(E_j) - A_{ex}^{CD}(E_j))^2 \quad (18)$

Note here that the  $E_j$ s represent energies in the relevant spectrum with an approximate spacing of 12.5 meV. For each term in the composite fitness equation, a perfect fit drives the fitness to zero.

## System Outputs

**Table S5:** Descriptions of key system outputs.

Aggregate parameter for TDM pair ( $m,n$ )	Description
Excitonic hopping parameter, $J_{m,n}$	Calculated excitonic hopping parameter for each pair of TDMs ( $m,n$ ) in the given orientation. [meV]
Center-to-center distance, $R_{m,n}$	The magnitude of a vector connecting the center points of each pair of TDMs ( $m,n$ ). [nm]
Oblique angle, $\alpha_{m,n}$	Total angle between each pair of TDMs in three dimensions given by the dot product between orientation vectors for each TDM pair. [degrees]
Twist angle, $\theta_t^{m,n}$	Angle of rotation of TDM $n$ with respect to TDM $m$ about the vector $\mathbf{R}$ connecting dye centers. A positive twist angle is reported as the clockwise rotation of TDM $n$ as viewed from TDM $m$ . [degrees]
Slip angle 1, $\theta_s^{m,R}$	Angle between TDM $m$ and the separation vector $\mathbf{R}_{m,n}$ . [degrees]
Slip angle 2, $\theta_s^{n,R}$	Angle between TDM $n$ and the separation vector $\mathbf{R}_{m,n}$ . [degrees]
X, Y, Z coordinates	Center positions for each TDM. [nm]
Zenith angle	Angle each TDM makes with the Z axis. [degrees]
Azimuthal angle	Angle each TDM projection makes in the XY plane measured counterclockwise from the X-axis. [degrees]

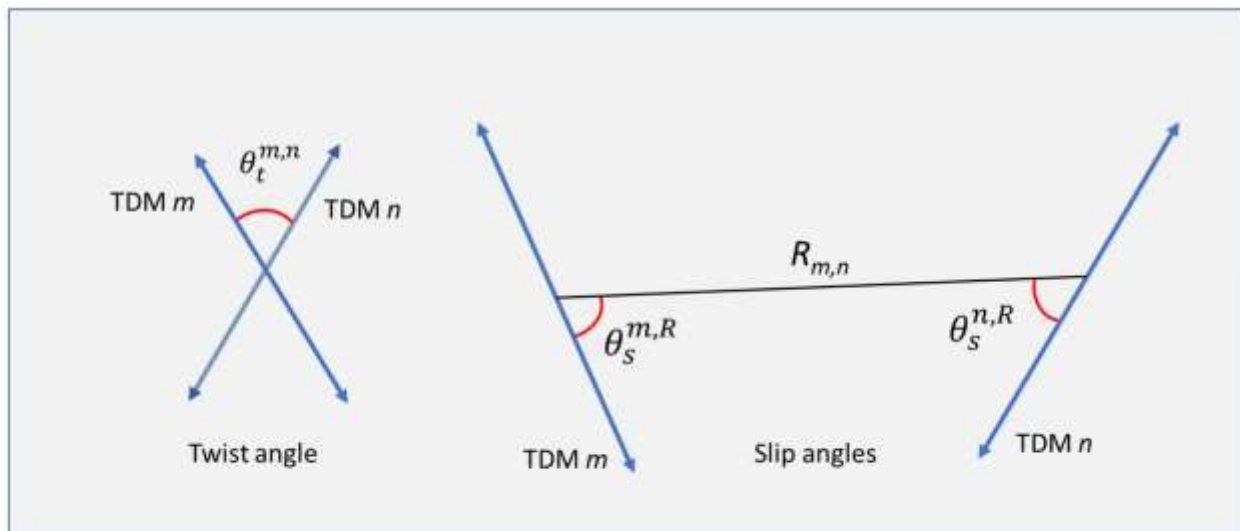


**Figure S22:** Diagrams depicting the twist angle about the separation vector and the two slip angles for each pair of TDMs. Slip angles range between  $0^\circ$  and  $90^\circ$ . The sign of the twist angle is given by the right-hand rule about the separation vector pointing from  $m$  to  $n$ .

### Results

**Tables S6-S14** summarize the KRM Model Simulation Tool results for aggregates in this study. The preceding sections provide detailed descriptions of inputs and outputs. Each table shows a diagram of the sequences and chromophore placement for each design. Insets in each table are plots comparing experimental absorbance and CD spectra (solid black lines) in  $M^{-1}cm^{-1}$ . Theoretical spectra from the KRM Model Simulation Tool appear as dotted red lines. Vertical bars represent energy eigenstates with heights related to the transition amplitudes  $\gamma_i$  and  $\gamma_i^{CD}$ . The theoretical spectra are composed of the sum of these transitions. The bars are divided into black and red segments to show the relative electronic (black) versus vibronic (red) character in each transition. Electronic here refers to transitions to states that do not include any quanta of vibration in the delocalized exciton. Note that model spectra and transition amplitudes are scaled to show relative contributions from each transition and should not be viewed as quantitative. Visual representations of each model result can be seen in **Figure S23**.

Table S6: Cy5 dimer on a DNA:DNA duplex.

DNA:DNA dimer								
Number of chromophores	2							
Number of vibrational levels considered, $n_v$	3							
Scaffold variant	DNA:DNA							
Monomer property								units
Energy of a vibron $E_V$	157							meV
Displacement of excited state potential, $d$ , from ground state potential (dimensionless)	0.78							
Energy loss parameter, $\Gamma$	39							meV
Characteristic excitonic hopping parameter, $J_0$	61.28							meV*nm <sup>3</sup>
Huang-Rhys factor (dimensionless)	0.3042							
Transition dipole moment, $\mu$	13.205							debye
TDM length, $l$	1.4							nm
Energy offset from monomer, $E_{of}$	-3							meV
Aggregate parameter	units	(1,2)						
Exciton hopping parameter, $J_{m,n}$	meV	62.7						
Center-to-center distance, $R_{m,n}$	nm	0.83						
Oblique angle, $\alpha_{m,n}$	degrees	37						
*Twist angle, $\theta_t^{m,n}$	degrees	1.7						
^Slip angle 1, $\theta_s^{m,R}$	degrees	80.5						
^Slip angle 2, $\theta_s^{n,R}$	degrees	62.5						
	Center coordinates (nm)			Angles (degrees)				
Chromophore number	X	Y	Z	Zenith	Azimuthal			
1	0	0	-0.416	99.5	0			
2	0	0	0.416	62.5	1.7			
Fitting parameters	RR	$OI_{ABS}$	$OI_{CD}$	$OI_{total}$	$ms_{ABS}$	$ms_{CD}$	Total	
Goodness of fit results	1.05	0.9864	0.7864	0.8864	0.3898	2.486	Fitness	
Fitness weight	1	0	0	n/a	20	1	10,2855	
* Twist angle is taken to be the angle between TDM projections in a plane normal to the separation vector, $R_{m,n}$								
^ The slip angle depends on the reference dye. Slip angle is the angle between the TDM vector and the separation vector from the reference chromophore								

**Table S7:** Cy5 dimer on a DNA:LNA duplex.

DNA:LNA dimer								
<b>Number of chromophores</b>	2							
<b>Number of vibrational levels considered, <math>n_v</math></b>	3							
<b>Scaffold variant</b>	DNA:LNA							
<b>Monomer property</b>								<b>units</b>
Energy of a vibron $\epsilon_v$	182							meV
Displacement of excited state potential, $d$ , from ground state potential (dimensionless)	0.74							
Energy loss parameter, $\Gamma$	42							meV
Characteristic excitonic hopping parameter, $J_\theta$	61.89							meV*nm <sup>3</sup>
Huang-Rhys factor (dimensionless)	0.2738							
Transition dipole moment, $\mu$	13.27							debye
TDM length, $l$	1.4	nm						
Energy offset from monomer, $E_{of}$	-31	meV						
<b>Aggregate parameter</b>	<b>units</b>	<b>(1,2)</b>						
Exciton hopping parameter, $J_{m,n}$	meV	88.9						
Center-to-center distance, $R_{m,n}$	nm	0.53						
Oblique angle, $\alpha_{m,n}$	degrees	14.1						
*Twist angle, $\theta_r^{m,n}$	degrees	1.8						
^Slip angle 1, $\theta_s^{m,R}$	degrees	89.9						
^Slip angle 2, $\theta_s^{n,R}$	degrees	76.1						
	<b>Center coordinates (nm)</b>			<b>Angles (degrees)</b>				
<b>Chromophore number</b>	<b>X</b>	<b>Y</b>	<b>Z</b>	<b>Zenith</b>	<b>Azimuthal</b>			
1	0	0	-0.267	90.1	0.0			
2	0	0	0.267	76.1	1.8			
<b>Fitting parameters</b>	<b>RR</b>	<b>OI<sub>ABS</sub></b>	<b>OI<sub>CD</sub></b>	<b>OI<sub>total</sub></b>	<b>ms<sub>ABS</sub></b>	<b>ms<sub>CD</sub></b>	<b>Total</b>	
Goodness of fit results	1.01	0.9710	0.7930	0.8220	1.076	3.046	Fitness	
Fitness weight	1	0	0	n/a	1	1	4.12242	
* Twist angle is taken to be the angle between TDM projections in a plane normal to the separation vector, $R_{m,n}$								
^ The slip angle depends on the reference dye. Slip angle is the angle between the TDM vector and the separation vector from the reference chromophore								

Table S8: Cy5 dimer on a DNA:BNA duplex.

DNA:BNA dimer									
Number of chromophores	2								
Number of vibrational levels considered, $n_v$	3								
Scaffold variant	DNA:BNA								
Monomer property								units	
Energy of a vibron $\mathcal{E}_v$	175							meV	
Displacement of excited state potential, $d$ , from ground state potential (dimensionless)	0.75								
Energy loss parameter, $f$	42							meV	
Characteristic excitonic hopping parameter, $J_0$	62.3							meV*nm <sup>3</sup>	
Huang-Rhys factor (dimensionless)	0.28125								
Transition dipole moment, $\mu$	13.312							debye	
TDM length, $l$	1.4	nm							
Energy offset from monomer, $E_{of}$	-33	meV							
Aggregate parameter		units		(1,2)					
Exciton hopping parameter, $J_{m,n}$	meV	72.6							
Center-to-center distance, $R_{m,n}$	nm	0.69							
Oblique angle, $\alpha_{m,n}$	degrees	26.3							
*Twist angle, $\theta_t^{m,n}$	degrees	3							
^Slip angle 1, $\theta_s^{m,R}$	degrees	84.1							
^Slip angle 2, $\theta_s^{n,R}$	degrees	69.8							
		Center coordinates (nm)			Angles (degrees)				
Chromophore number		X	Y	Z	Zenith	Azimuthal			
1		0	0	-0.347	84.1	0.0			
2		0	0	0.347	110.2	3.0			
Fitting parameters		RR	OI <sub>ABS</sub>	OI <sub>CD</sub>	OI <sub>total</sub>	ms <sub>ABS</sub>	ms <sub>CD</sub>	Total	
Goodness of fit results		0.993	0.9824	0.8831	0.9328	0.5476	1.664	Fitness	
Fitness weight		1	0	0	n/a	1	1	2.21191	
* Twist angle is taken to be the angle between TDM projections in a plane normal to the separation vector, $R_{m,n}$									
^ The slip angle depends on the reference dye. Slip angle is the angle between the TDM vector and the separation vector from the reference chromophore									



Table S9: Cy5 trimer on a DNA:DNA duplex.

DNA:DNA trimer								
Number of chromophores	3							
Number of vibrational levels considered, $n_v$	3							
Scaffold variant	DNA:DNA							
Monomer property							units	
Energy of a vibron $E_v$	157						meV	
Displacement of excited state potential, $d$ , from ground state potential (dimensionless)	0.78							
Energy loss parameter, $\Gamma$	39						meV	
Characteristic excitonic hopping parameter, $J_0$	61.3						meV*nm <sup>3</sup>	
Huang-Rhys factor (dimensionless)	0.30							
Transition dipole moment, $\mu$	13.205						debye	
TDM length, $l$	1.4	nm						
Energy offset from monomer, $E_{of}$	-22	meV						
Aggregate parameter	units	(1,2)	(1,3)	(2,3)				
Exciton hopping parameter, $J_{m,n}$	meV	52.6	14.3	44				
Center-to-center distance, $R_{m,n}$	nm	0.61	1.17	0.73				
Oblique angle, $\alpha_{m,n}$	degrees	35.1	42.7	48.5				
*Twist angle, $\theta_{\tau}^{m,n}$	degrees	29.5	20.1	-34.2				
^Slip angle 1, $\theta_s^{m,R}$	degrees	50.7	73.9	89.3				
^Slip angle 2, $\theta_s^{n,R}$	degrees	74.5	34.3	52.3				
		Center coordinates (nm)			Angles (degrees)			
Chromophore number		X	Y	Z	Zenith	Azimuthal		
1		0.833	-0.090	0.917	100.1	-19.9		
2		0.414	-0.296	1.315	65.6	-13.2		
3		0.231	-1.003	1.328	98.4	23.4		
Fitting parameters		$RR$	$OI_{ABS}$	$OI_{CD}$	$OI_{total}$	$ms_{ABS}$	$ms_{CD}$	Total
Goodness of fit results		1.01	0.9775	0.990	0.9839	0.7463	0.1198	Fitness
Fitness weight		1	0	0	n/a	1	1	0.86619
* Twist angle is taken to be the angle between TDM projections in a plane normal to the separation vector, $R_{m,n}$								
^ The slip angle depends on the reference dye. Slip angle is the angle between the TDM vector and the separation vector from the reference chromophore								

Table S10: Cy5 trimer on a DNA:LNA duplex.

DNA:LNA trimer											
Number of chromophores	3										
Number of vibrational levels considered, $n_v$	3										
Scaffold variant	DNA:LNA										
Monomer property								units			
Energy of a vibron $E_v$	182							meV			
Displacement of excited state potential, $d$ , from ground state potential (dimensionless)	0.74										
Energy loss parameter, $\Gamma$	42							meV			
Characteristic excitonic hopping parameter, $f_0$	61.9							$\text{meV} \cdot \text{nm}^3$			
Huang-Rhys factor (dimensionless)	0.2738										
Transition dipole moment, $\mu$	13.271							debye			
TDM length, $l$	1.4	nm									
Energy offset from monomer, $E_{of}$	-15	meV									
Aggregate parameter		units		(1,2)	(1,3)	(2,3)					
Exciton hopping parameter, $J_{m,n}$	meV	91.0	20.0	61.0							
Center-to-center distance, $R_{m,n}$	nm	0.45	1.27	0.86							
Oblique angle, $\alpha_{m,n}$	degrees	12.5	36.2	40.1							
*Twist angle, $\theta_z^{m,n}$	degrees	12.6	3.7	-7.6							
^Slip angle 1, $\theta_s^{m,R}$	degrees	74.3	87.2	74.3							
^Slip angle 2, $\theta_s^{n,R}$	degrees	77.1	56.7	66.3							
		Center coordinates (nm)			Angles (degrees)						
Chromophore number		X	Y	Z	Zenith	Azimuthal					
1		1.307	0.798	0.021	76.0	-4.6					
2		1.096	0.909	0.399	76.6	8.2					
3		1.102	1.182	1.217	111.5	-11.8					
Fitting parameters		RR	$OI_{ABS}$	$OI_{CD}$	$OI_{total}$	$ms_{ABS}$	$ms_{CD}$	Total			
Goodness of fit results		1.12	0.9697	0.9381	0.9539	1.129	1.231	Fitness			
Fitness weight		1	0	0	n/a	1	1	2.37551			
* Twist angle is taken to be the angle between TDM projections in a plane normal to the separation vector, $R_{m,n}$											
^ The slip angle depends on the reference dye. Slip angle is the angle between the TDM vector and the separation vector from the reference chromophore											

Table S11: Cy5 trimer on a DNA:BNA duplex.

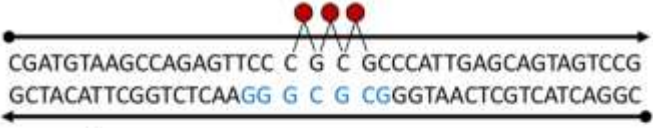
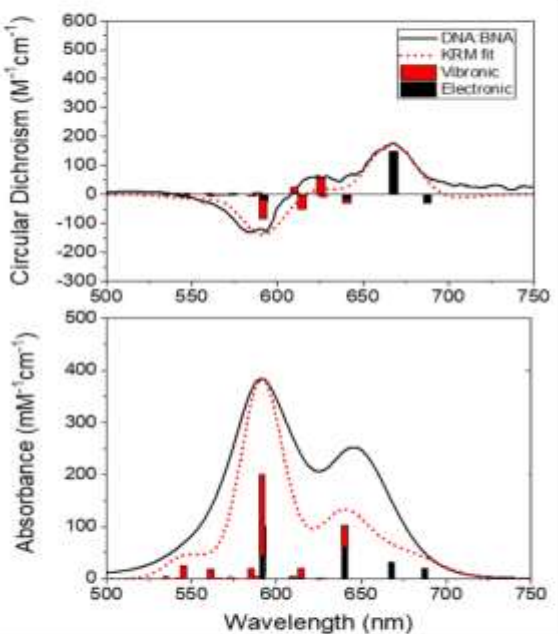
DNA:BNA trimer							
Number of chromophores	3						
Number of vibrational levels considered, $n_v$	3						
Scaffold variant	DNA:BNA						
Monomer property							units
Energy of a vibron $E_v$	175						meV
Displacement of excited state potential, $d$ , from ground state potential (dimensionless)	0.75						
Energy loss parameter, $\Gamma$	42						meV
Characteristic excitonic hopping parameter, $J_\theta$	62.3						meV*nm <sup>3</sup>
Huang-Rhys factor (dimensionless)	0.28125						
Transition dipole moment, $\mu$	13.312						debye
TDM length, $l$	1.4	nm					
Energy offset from monomer, $E_{of}$	-33	meV					
Aggregate parameter	units	(1,2)	(1,3)	(2,3)			
Exciton hopping parameter, $J_{m,n}$	meV	73.6	39.1	93.0			
Center-to-center distance, $R_{m,n}$	nm	0.68	1.00	0.36			
Oblique angle, $\alpha_{m,n}$	degrees	36.9	36.6	25.2			
*Twist angle, $\theta_t^{m,n}$	degrees	-18.2	6.8	24.7			
^Slip angle 1, $\theta_s^{m,R}$	degrees	80.1	70.0	81.5			
^Slip angle 2, $\theta_s^{n,R}$	degrees	67.6	74.0	87.2			
Chromophore number	Center coordinates (nm)			Angles (degrees)			
	X	Y	Z	Zenith	Azimuthal		
	1	0.981	-0.591	0.298	70.3		2.0
	2	0.884	-0.810	0.935	106.6		-4.3
3	1.020	-0.939	1.238	101.6	21.2		
Fitting parameters	RR	OI <sub>ABS</sub>	OI <sub>CD</sub>	OI <sub>total</sub>	ms <sub>ABS</sub>	ms <sub>CD</sub>	Total Fitness
Goodness of fit results	1.04	0.9548	0.9204	0.9376	1.824	1.444	3.26974
Fitness weight	1	0	0	n/a	1	1	
* Twist angle is taken to be the angle between TDM projections in a plane normal to the separation vector, $R_{m,n}$							
^ The slip angle depends on the reference dye. Slip angle is the angle between the TDM vector and the separation vector from the reference chromophore							

Table S12: Cy5 tetramer on a DNA:DNA duplex.

DNA:DNA tetramer								
		Number of chromophores	4					
Number of vibrational levels considered, $n_v$	3							
Scaffold variant	DNA:DNA							
Monomer property		units						
Energy of a vibron $E_v$	157	meV						
Displacement of excited state potential, $d$ , from ground state potential (dimensionless)	0.78							
Energy loss parameter, $\Gamma$	39	meV						
Characteristic excitonic hopping parameter, $J_0$	61.3	meV*nm <sup>3</sup>						
Huang-Rhys factor (dimensionless)	0.3042							
Transition dipole moment, $\mu$	13.205	debye						
TDM length, $l$	1.4	nm						
Energy offset from monomer, $E_{of}$	-22	meV						
Aggregate parameter		units	(1,2)	(1,3)	(2,3)	(1,4)	(2,4)	(3,4)
Exciton hopping parameter, $J_{m,n}$	meV	60.5	20.0	54.1	1.7	3.0	4.4	
Center-to-center distance, $R_{m,n}$	nm	0.61	1.17	0.68	3.10	2.56	2.19	
Oblique angle, $\alpha_{m,n}$	degrees	3.3	12.9	14.1	4.9	7.8	15.2	
*Twist angle, $\theta_t^{m,n}$	degrees	-3.5	3.7	4.2	1.9	4.3	-11.1	
^Slip angle 1, $\theta_s^{m,R}$	degrees	64.2	85.8	75.6	83.1	89.5	88.2	
^Slip angle 2, $\theta_s^{n,R}$	degrees	65.2	81.9	62.1	78.6	83.0	77.7	
		Center coordinates (nm)			Angles (degrees)			
Chromophore number		X	Y	Z	Zenith	Azimuthal		
1		0.827	-1.298	-0.499	93.6	-5.4		
2		0.615	-1.091	0.028	91.6	-8.0		
3		0.865	-0.610	0.443	85.9	4.9		
4		0.676	-1.028	2.587	98.3	-3.9		
Fitting parameters		RR	OI <sub>ABS</sub>	OI <sub>CD</sub>	OI <sub>total</sub>	ms <sub>ABS</sub>	ms <sub>CD</sub>	Total
Goodness of fit results		1.03	0.9575	0.9553	0.9564	1.613	0.5000	Fitness
Fitness weight		1	0	0	n/a	1	1	2.11383
* Twist angle is taken to be the angle between TDM projections in a plane normal to the separation vector, $R_{m,n}$								
^ The slip angle depends on the reference dye. Slip angle is the angle between the TDM vector and the separation vector from the reference chromophore								

Table S13: Cy5 tetramer on a DNA:LNA duplex.

DNA:LNA tetramer								
Number of chromophores	4							
Number of vibrational levels considered, $n_v$	3							
Scaffold variant	DNA:LNA							
Monomer property								units
Energy of a vibron $E_v$	182							meV
Displacement of excited state potential, $d$ , from ground state potential (dimensionless)	0.74							
Energy loss parameter, $F$	42							meV
Characteristic excitonic hopping parameter, $J_0$	61.9							meV*nm <sup>3</sup>
Huang-Rhys factor (dimensionless)	0.2738							
Transition dipole moment, $\mu$	13.271							debye
TDM length, $l$	1.4	nm						
Energy offset from monomer, $E_{of}$	-40	meV						
Aggregate parameter	units	(1,2)	(1,3)	(2,3)	(1,4)	(2,4)	(3,4)	
Exciton hopping parameter, $J_{m,n}$	meV	8.5	5.3	109.5	3.5	34.1	93.2	
Center-to-center distance, $R_{m,n}$	nm	1.70	2.05	0.41	2.43	0.90	0.50	
Oblique angle, $\alpha_{m,n}$	degrees	9.5	6.8	5.4	6.9	12.5	12.5	
*Twist angle, $\theta_j^{m,n}$	degrees	-3.3	-5	-4.7	6.8	1.9	5.5	
^Slip angle 1, $\theta_s^{m,R}$	degrees	89.0	89.3	80.2	90.0	79.5	80.4	
^Slip angle 2, $\theta_s^{n,R}$	degrees	82.1	86.1	83.0	89.6	88.1	88.4	
Chromophore number	Center coordinates (nm)			Angles (degrees)				
	X	Y	Z	Zenith	Azimuthal			
1	1.031	0.967	-0.553	90.6	-1.0			
2	1.029	1.554	1.046	81.1	-1.0			
3	1.036	1.450	1.444	85.0	-4.8			
4	1.060	1.188	1.866	91.7	5.8			
Fitting parameters	RR	OI <sub>ABS</sub>	OI <sub>CD</sub>	OI <sub>total</sub>	ms <sub>ABS</sub>	ms <sub>CD</sub>	Total Fitness	
Goodness of fit results	0.683	0.939	0.7991	0.8691	2.702	3.922		
Fitness weight	1	0	0	n/a	1	1	6.27245	
* Twist angle is taken to be the angle between TDM projections in a plane normal to the separation vector, $R_{m,n}$								
^ The slip angle depends on the reference dye. Slip angle is the angle between the TDM vector and the separation vector from the reference chromophore								

**Table S14:** Cy5 tetramer on a DNA:BNA duplex.

DNA:BNA tetramer								
Number of chromophores	4							
Number of vibrational levels considered, $n_v$	3							
Scaffold variant	DNA:BNA							
Monomer property	units							
Energy of a vibron $E_v$	175							meV
Displacement of excited state potential, $d$ , from ground state potential (dimensionless)	0.75							
Energy loss parameter, $\Gamma$	42							meV
Characteristic excitonic hopping parameter, $J_0$	62.3							meV*nm <sup>3</sup>
Huang-Rhys factor (dimensionless)	0.28125							
Transition dipole moment, $\mu$	13.312							debye
TDM length, $l$	1.4	nm						
Energy offset from monomer, $E_{of}$	-25	meV						
Aggregate parameter	units	(1,2)	(1,3)	(2,3)	(1,4)	(2,4)	(3,4)	
Exciton hopping parameter, $J_{m,n}$	meV	135.4	35.3	79.4	2.4	2.7	3.3	
Center-to-center distance, $R_{m,n}$	nm	0.35	0.93	0.60	2.79	2.68	2.43	
Oblique angle, $\alpha_{m,n}$	degrees	5.0	21.5	21.8	6.7	2.3	20.3	
*Twist angle, $\theta_t^{m,n}$	degrees	-5.0	2.7	9.6	-0.7	1.4	-19.8	
^Slip angle 1, $\theta_s^{m,R}$	degrees	88.2	81.1	78.5	85.4	89.7	89.7	
^Slip angle 2, $\theta_s^{n,R}$	degrees	88.2	77.6	98.1	88.0	87.9	85.4	
Chromophore number	Center coordinates (nm)			Angles (degrees)				
	X	Y	Z	Zenith	Azimuthal			
	1	1.017	0.866	-1.237	80.9	-4.6		
	2	0.968	0.643	-0.973	84.2	-8.4		
	3	0.996	0.392	-0.431	97.9	8.5		
4	0.952	2.155	1.236	86.5	-8.3			
Fitting parameters	RR	OI <sub>ABS</sub>	OI <sub>CD</sub>	OI <sub>total</sub>	ms <sub>ABS</sub>	ms <sub>CD</sub>	Total Fitness	
Goodness of fit results	1.07	0.9131	0.8647	0.8889	3.509	3.164		
Fitness weight	1	0	0	n/a	1	1	6.67774	
* Twist angle is taken to be the angle between TDM projections in a plane normal to the separation vector, $R_{m,n}$								
^ The slip angle depends on the reference dye. Slip angle is the angle between the TDM vector and the separation vector from the reference chromophore								

*Visualizing Model Results*

Results from the KRM Model Simulation Tool were used to create visual representations of each aggregate. Vector renditions of TDMs were plotted using Origin (2019b). Center positions and orientation angles in **Tables S6-S14** were used to locate and orient each TDM in 3D space. Projections of each TDM appear on the planes of the axes to assist with interpretation. Molecular images were created using the chemical structure of a Cy5 molecule assembled and manipulated using Avogadro. TDMs are assumed to run along the long axis of each chromophore. Orientation angles and center positions were used to orient each chromophore image according to the KRM Model Simulation Tool outputs. Oriented chromophore images were imported into Chimera to produce the molecular images shown in **Figures S23-S25**.

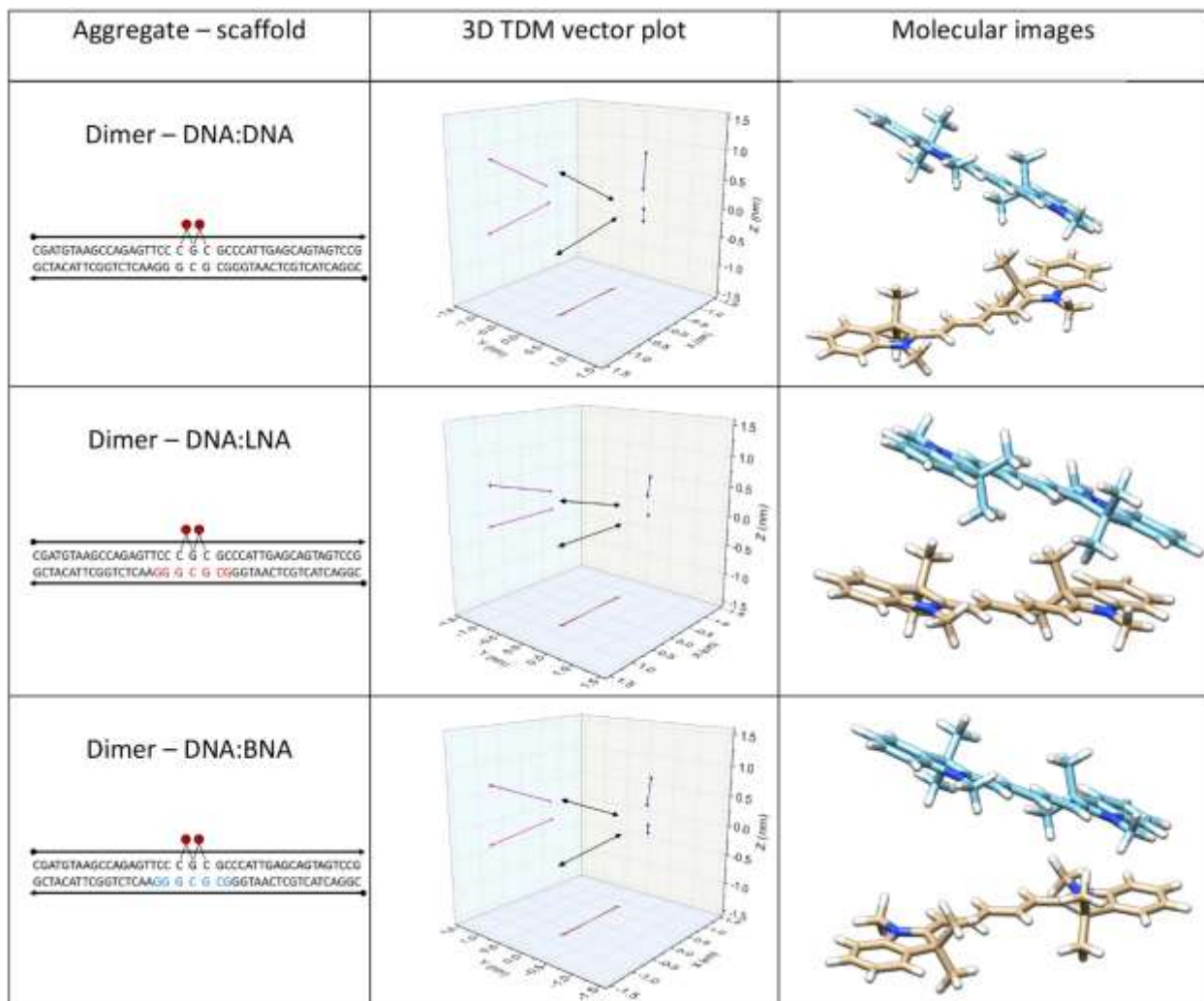


**Figure S23:** Visual representations of each dimer aggregate-scaffold combination (left column). Based on KRM Simulation Tool outputs, vector plots (center column) were created in Origin Pro (2019b). The TDM for each chromophore in each aggregate is represented in three dimensions by a double-headed black vector that was then projected onto each axis plane (colored arrows) to aid visual interpretation. Molecular images (right column) were created using Avogadro and visualized using Chimera<sup>7</sup>. Molecular image models were arranged assuming the TDMs span the long axis of each chromophore. Note that the current KRM Model Simulation Tool does not provide information about the orientation of the plane of the chromophore about the TDM axis.



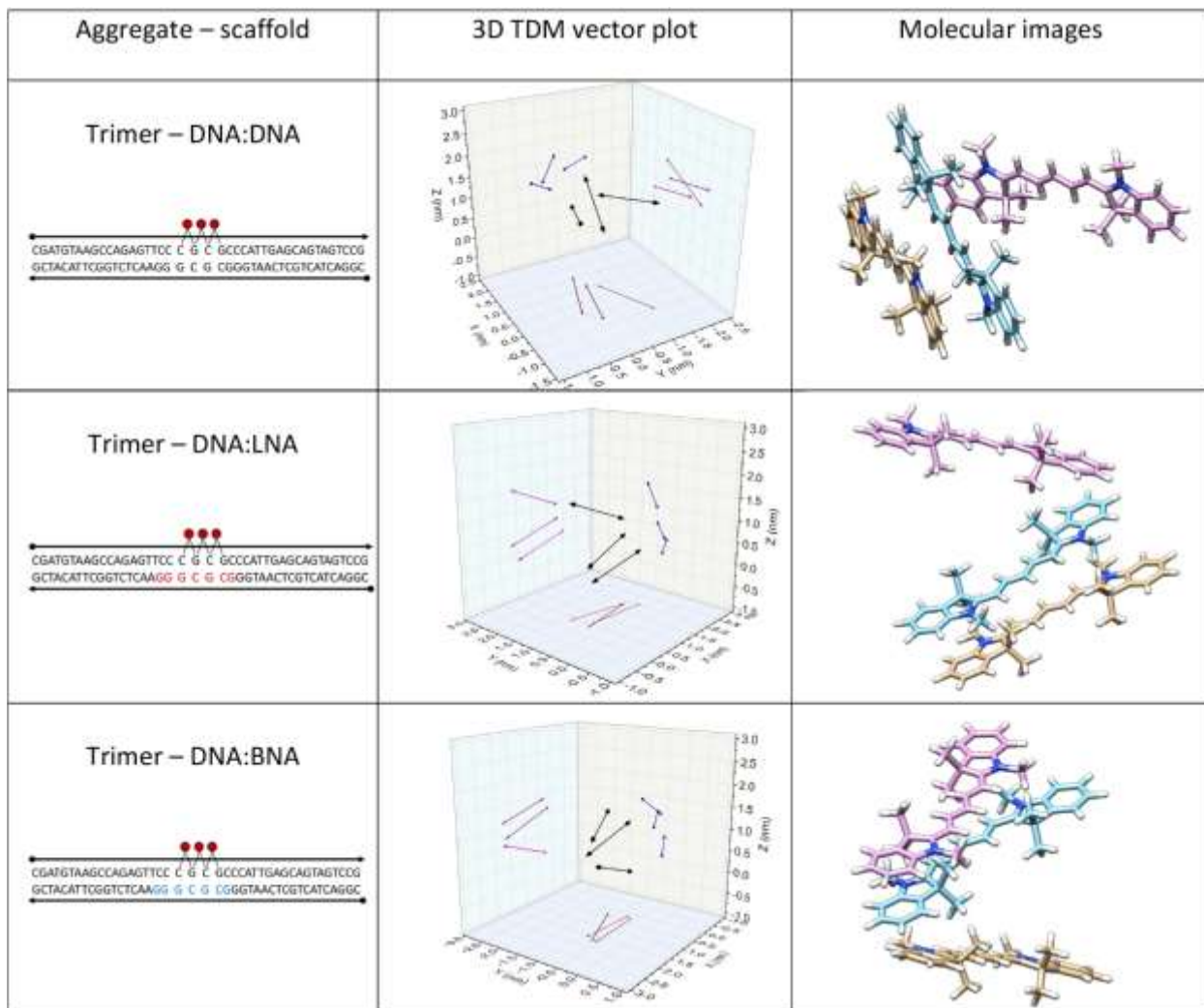


**Figure S24:** Visual representations of each trimer aggregate-scaffold combination (left column). Based on KRM Simulation Tool outputs, vector plots (center column) were created in Origin Pro (2019b). The TDM for each chromophore in each aggregate is represented in three dimensions by a double-headed black vector that was then projected onto each axis plane (colored arrows) to aid visual interpretation. Molecular images (right column) were created using Avogadro and visualized using Chimera<sup>7</sup>. Molecular image models were arranged assuming the TDMs span the long axis of each chromophore. Note that the current KRM Model Simulation Tool does not provide information about the orientation of the plane of the chromophore about the TDM axis.

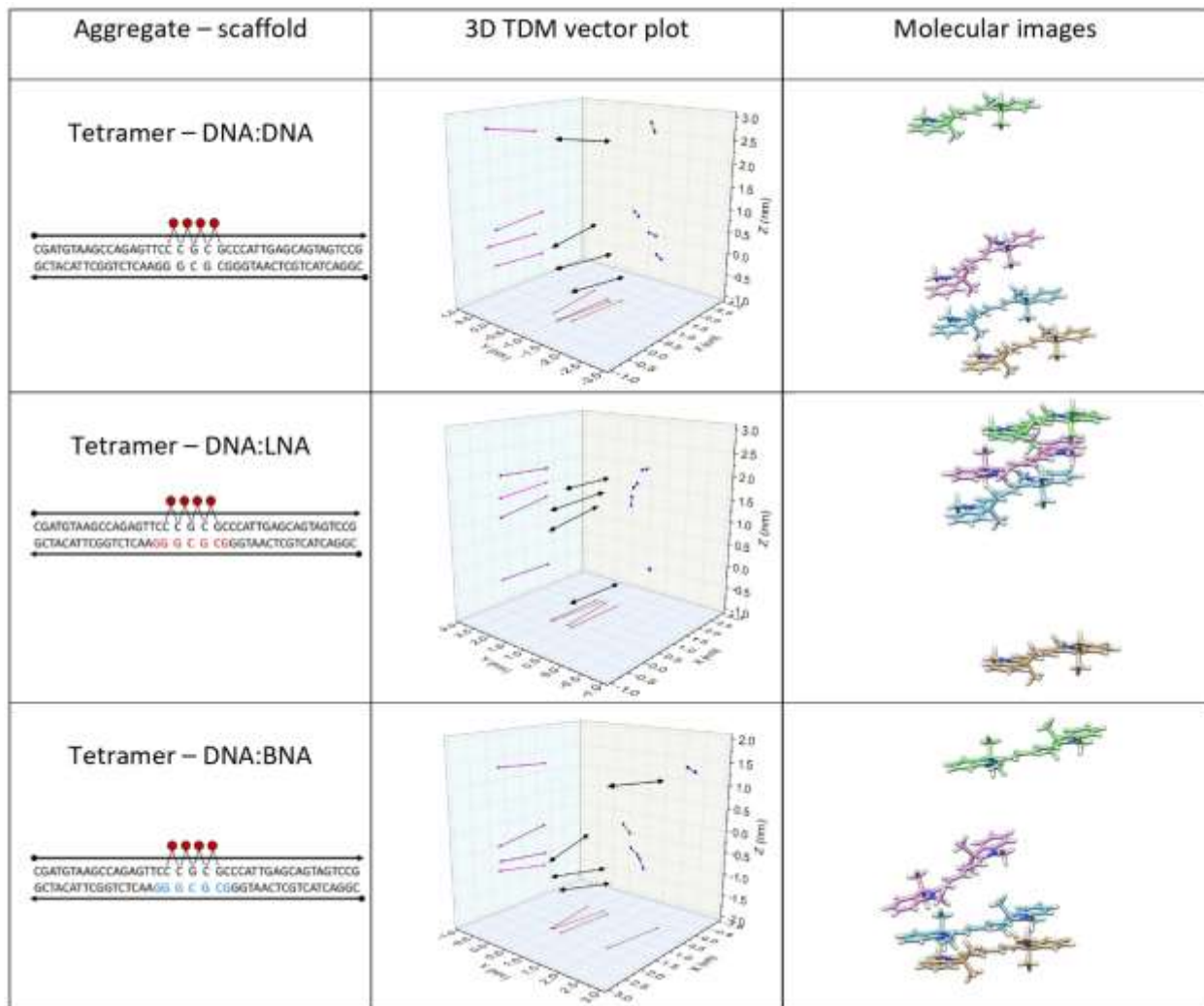


**Figure S25:** Visual representations of each tetramer aggregate-scaffold combination (left column). Based on KRM Simulation Tool outputs, vector plots (center column) were created in Origin Pro (2019b). The TDM for each chromophore in each aggregate is represented in three dimensions by a double-headed black vector that was then projected onto each axis plane (colored arrows) to aid visual interpretation. Molecular images (right column) were created using Avogadro and visualized using Chimera<sup>7</sup>. Molecular image models were arranged assuming the TDMs span the long axis of each chromophore. Note that the current KRM Model Simulation Tool does not provide information about the orientation of the plane of the chromophore about the TDM axis.

#### S14: Vibrational Coupling in Steady-State Optical Spectra

The KRM Model Simulation Tool was used to assess the influence of coupling electronic states to vibrational states in steady-state absorbance and CD spectra. The relevant parameter within the model is the Huang-Rhys<sup>8</sup> (H-R) factor (see **Table S3**). The H-R factor is a dimensionless parameter related to the displacement of harmonic oscillator energy surfaces (**Figure S20**) and the vibrational energy of the system and is used to model the system. As the H-R factor increases, the coupling between electronic and vibrational excited states increases.

To study the effect of varying the H-R factor, a fixed orientation was selected, and all other parameters were held constant (see **Table S6**). For simplicity and relevance, the modeling results from a Cy5 dimer on a purely DNA duplex were used to examine changes in coupling as the H-R factor was increased from zero (no vibrational coupling) to one. A schematic of the DNA:DNA dimer and the resulting KRM Model Simulation Tool orientations are shown in **Figure S26**. Theoretical spectra obtained while varying the H-R factor are shown in **Figures S27** and **S28**.

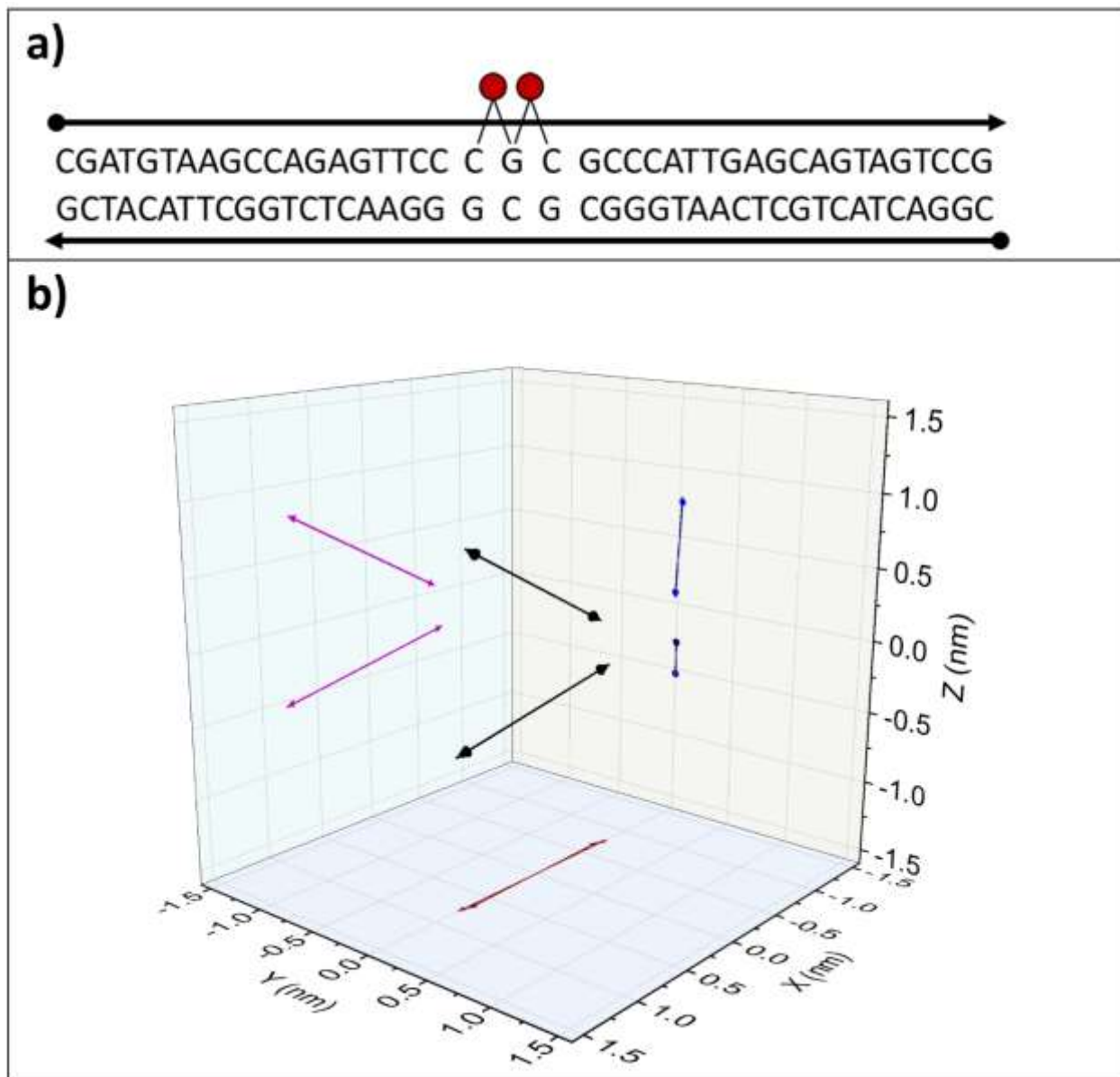


**Figure S26:** Example of an H-like dimer arrangement that is typical of the aggregates in this study. These images are repeated from **Figure S23** for easy reference with **a)** sequences and dye placement for a Cy5 dimer on a purely DNA duplex and **b)** TDM vector orientations obtained from the KRM Model Simulation Tool. This transition dipole orientation was used to explore the influence of the H-R factor in our resulting model spectra.

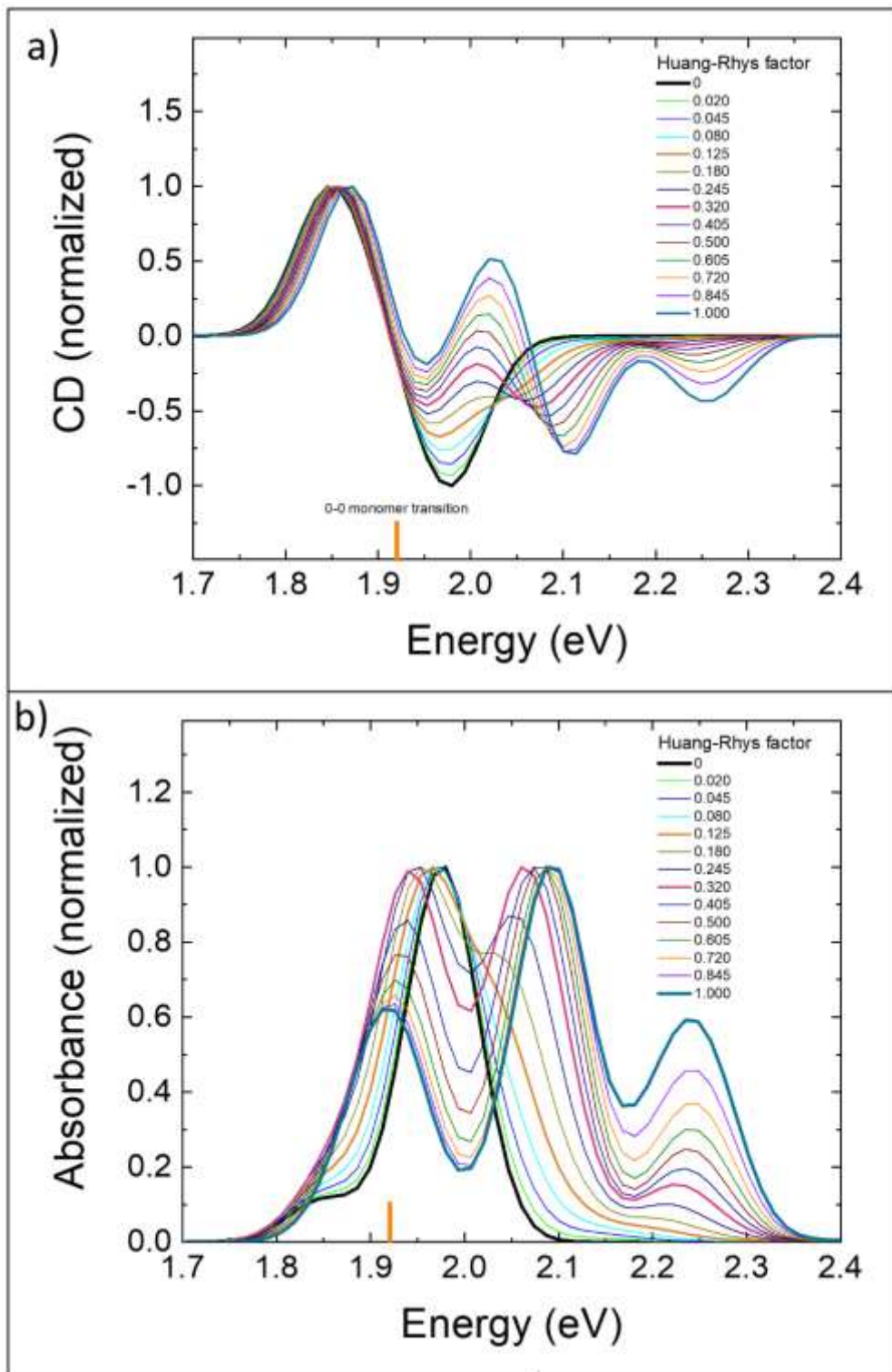


**Figure S27:** Calculated **a)** normalized CD and **b)** normalized absorbance spectra for increasing H-R factors starting from zero. Aside from the H-R factor, the TDM orientations and monomer properties reported in **Table S6** were held fixed. The vertical orange stick represents the 0-0 monomer transition energy of 1.92 eV.

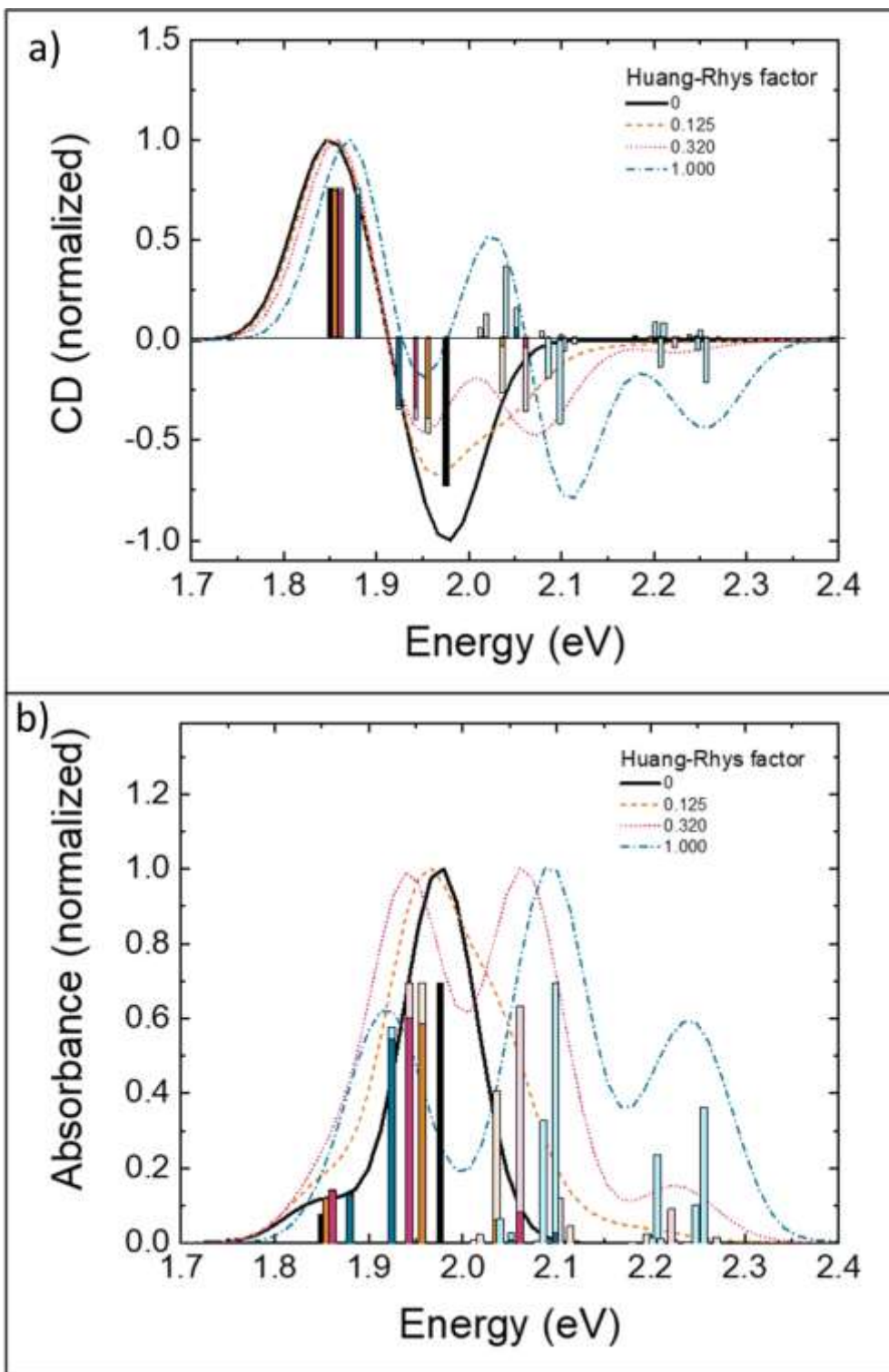


**Figure S28** shows a selection of the curves from **Figure S27** for closer analysis. Vertical bars represent the relative electronic (darker shade corresponding to curve color) versus vibronic (lighter shade) content in each absorption band in the **a)** circular dichroism and **b)** absorbance spectra.

### Discussion

The bold black traces shown in both panels of **Figures S27** and **S28** show the spectra arising from the orientation given in **Figure S26** when no vibrational coupling is considered. For Cy5 on this specific scaffold, the 0-0 monomer peak is located at 1.92 eV. The black traces in the absorbance spectra are composed of two absorption bands centered at 1.851 eV and 1.976 eV indicative of Davydov splitting of 125 meV. The lower energy band is suppressed in the absorbance spectrum due to symmetry considerations in the H-like (nearly face-to-face) stacking arrangement (**Figure S26b**). For perfectly parallel TDMs in a face-to-face arrangement, one would expect the lower energy peak to vanish from the absorbance spectrum. In contrast, the corresponding black trace in the CD spectrum shows a perfect couplet (Cotton effect) with no suppression of the lower energy band. The lower energy CD band was not suppressed by the H-like geometry because the selection rules for CD transitions are fundamentally different from linear absorbance transitions due to the importance of magnetic dipoles in CD spectroscopy<sup>9</sup>. The difference in selection rules between linear absorbance and circular dichroism results in observed CD features at energies below the lowest electronic monomer transition in the associated monomer because the transitions associated with the lowest energy CD features are suppressed in the linear absorbance spectrum for H-like aggregates.

As the H-R factor increased from zero, additional (vibronic) features appeared in the absorbance and CD spectra. For a closer analysis, **Figure S28** compares spectra for H-R factors = {0, 0.125, 0.320, 1}. With an H-R factor of 0.125, an additional strong absorbance band appeared at ~2.03 eV that is nearly entirely vibronic in nature (that is, the transition includes at least one quantum of vibration). As the H-R factor increased, this vibronic peak appeared to have blue-shifted up to ~2.10 eV at H-R = 1. In addition to the prominent vibronic transition, several weaker vibronic features developed in the 2.10-2.20 eV range at lower H-R factors. As the H-R factor approaches 1, these weaker vibronic transitions grew to significantly impact the resulting spectra. We also noted small incremental decreases in the splitting initially observed in the H-R = 0 case (**Table S15**).

**Table S15:** Difference in energy between the two lowest absorption and CD features in the spectra for the selected H-R factors shown in **Figure S28**.

Huang-Rhys factor	Energy difference between two lowest absorption bands (meV)
0	125
0.125	101
0.320	81
1	44

We note that as the H-R factor increased, the two lowest energy absorbance (CD) bands remained almost entirely electronic as indicated by the darker portions of the stick plots in **Figure S28**. Additionally, even though the absorbance of the lowest state is suppressed by the packing orientation, the lowest energy band remained as the strongest feature in the CD spectrum.

When the H-R became sufficiently high, the two lowest energy absorption bands merged into a composite peak and became unresolvable. The strong higher energy bands seen in the absorbance spectra with high H-R factors (e.g., when H-R factor = 1) were mostly vibrational in character, and the corresponding CD spectra became increasingly complex. The multiple observed features in the experimental CD spectra in this study were at least in part attributable to coupling to vibrational modes.

## S15: Ultra-Violet Circular Dichroism

To further evaluate changes to the DNA scaffold induced by inclusion of bridged nucleotides, we performed a qualitative analysis to estimate the fraction of the DNA helix that is perturbed toward an A-form-like conformation. The CD spectra in **Figure S29a** were extracted from a textbook chapter entitled “Circular Dichroism Spectroscopy of Nucleic Acids”<sup>10</sup> using WebPlotDigitizer<sup>11</sup> to represent the CD spectra of typical A-form and B-form DNA in molar extinction units (see **Figure S29**).

To compare these spectra with our experimental results, we combined linear combinations of these spectra to approximate expected CD spectra from structures that have a mixture of A-form and B-form DNA. Spectra were weighted by a series of fractions to represent a range of A-form content in an otherwise B-form helix and summed to produce a combined spectrum. The resulting spectrum was normalized such that the maximum positive value = 1 to compare with our experimental results. **Figure S29b** shows expected (normalized) spectra covering the entire range between A-form and B-form DNA to show the incremental transition as the percentage of A-form increases.

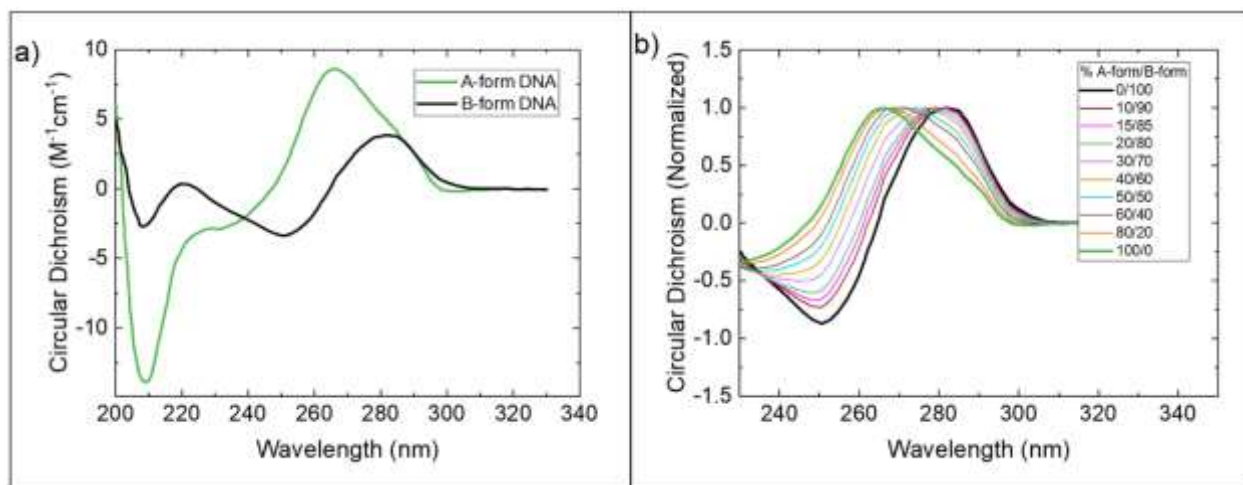


**Figure S29:** **a)** Representative CD spectra for A-form and B-form DNA in molar extinction units as extracted from the literature.<sup>10,11</sup> **b)** Normalized (theoretical) CD spectra for a range of A-form content from 0 to 100% A-form DNA. Here we focus on the region > 230nm because our experimental data are unusable at shorter wavelengths due to scattering from Mg ions in the buffer.

Previous molecular dynamics results reported by Ivanova and Rösch<sup>12</sup> suggest that the perturbation of the helix from inclusion of bridged nucleotides is localized near the synthetic nucleotides. Based on this idea, we expect that our 42 bp DNA duplex (including seven consecutive bridged nucleotides) may have between (roughly) five and nine base pairs that adopt an A-form-like helix conformation. This suggests that we might expect between 12% and 22% A-form-like content in our otherwise B-form DNA helix.

### Results and Discussion

Our experimental CD results for the unmodified DNA duplex closely agreed with the previously published spectra<sup>10</sup> (see **Figure S30a**), indicating that the sample contained a canonical B-form DNA duplex. Experimental results for unlabeled DNA with bridged nucleotide substitutions showed shifts from the unmodified spectrum that were consistent with our theoretical spectrum for a 15/85% (A-form/B-form) mixture.



All dye-labeled structures appeared to follow the same trend as seen in the unlabeled samples. The spectra from samples without bridged nucleotides resembled the purely B-form spectra, whereas the spectra from samples including either BNA or LNA appeared to be consistent with a mixed spectrum with approximately 15% A-form content. These results are consistent with the idea that the DNA structure, in all cases, is perturbed by the bridged nucleotides to adopt an A-form-like character in the domain of the attached chromophores. These results also agree with our conclusion from our theoretical melting points of duplex fragments (see main text) that base hybridization was occurring to a certain extent between the base pairs within the domain containing the chromophores.

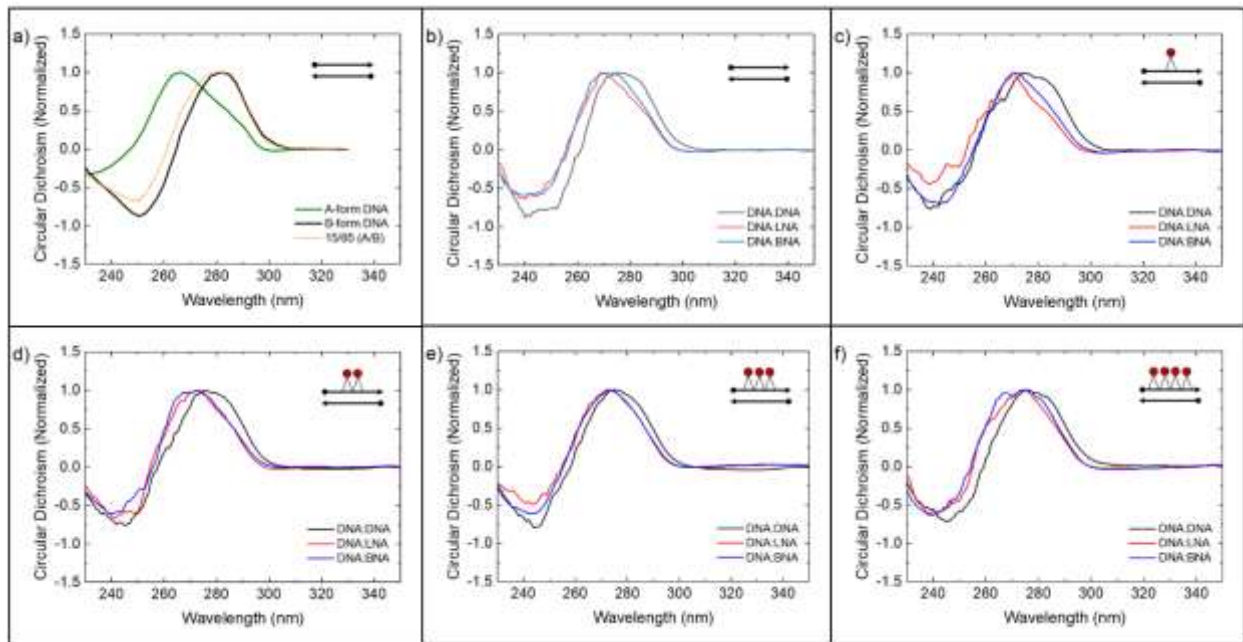


**Figure S30:** **a)** Theoretical A-form and B-form normalized CD spectra compared with a combined 15/85% (normalized) linear combination of the two curves in **Figure S29a**. Normalized experimental CD spectra from **b)** unlabeled 42 bp duplex **c)** monomers, **d)** dimers, **e)** trimers, and **f)** tetramers with only DNA (**black**), seven substituted LNA nucleotides (**red**), and seven substituted BNA nucleotides (**blue**). All samples were prepared to a nominal 5 $\mu$ M in 1 $\times$  TBE with 15mM added MgCl<sub>2</sub>. Insets in each panel denote the number of chromophores present for each duplex design.

### SI6: Steady-State Fluorescence

To further characterize the electronic behavior of the aggregates in this study, we performed steady-state fluorescence measurements. Samples were prepared at 1  $\mu$ M in 1 $\times$  TBE with 15mM added  $MgCl_2$ . Fluorescence spectra were collected with a Horiba Fluorolog 3 spectrophotometer using a 1 cm pathlength quartz cuvette (50  $\mu$ L; Starna). Samples were excited at 608 nm with a 5 nm excitation slit and a 3 nm emission slit. Emission was swept from 615 nm to 800 nm at 23  $^{\circ}$ C. Data were processed by subtracting a buffer signal and corrected for instrument response using data provided by the manufacturer. Data were scaled by dividing by absorbance at the excitation wavelength and subsequently normalized with respect to the monomer on DNA:DNA.

**Figure S31** gives a summary of fluorescence results arranged by number of chromophores. Monomer constructs that included LNA or BNA showed a decreased relative fluorescence compared to their DNA:DNA equivalent. We suspect local interactions between the chromophores and DNA bases are affected by the altered base stacking associated with A-form-like DNA, leading to a subtle change in fluorescence behavior. In all cases, constructs with two chromophores showed an 85-90% decrease in relative fluorescence, and each added chromophore led to decreased fluorescence. Trimer constructs showed a 93-95% decrease in fluorescence, whereas tetramers showed roughly 97% quenching. We note that the tetramer signal was nearly too low for measurement and should be considered as qualitative.

The consistent strong fluorescence quenching and the clear trend of additional chromophores leading to fewer emitted photons leads to two conclusions: 1) All of the chromophores within our samples are interacting with each other in some way. 2) The inter-chromophore interactions apparently lead to extreme quenching of fluorescence in all multi-chromophore samples; this is consistent with the expectation of sub-radiance in H-like aggregates. These conclusions support our finding that the chromophore aggregates in this study adopted face-to-face, H-like packing orientation.

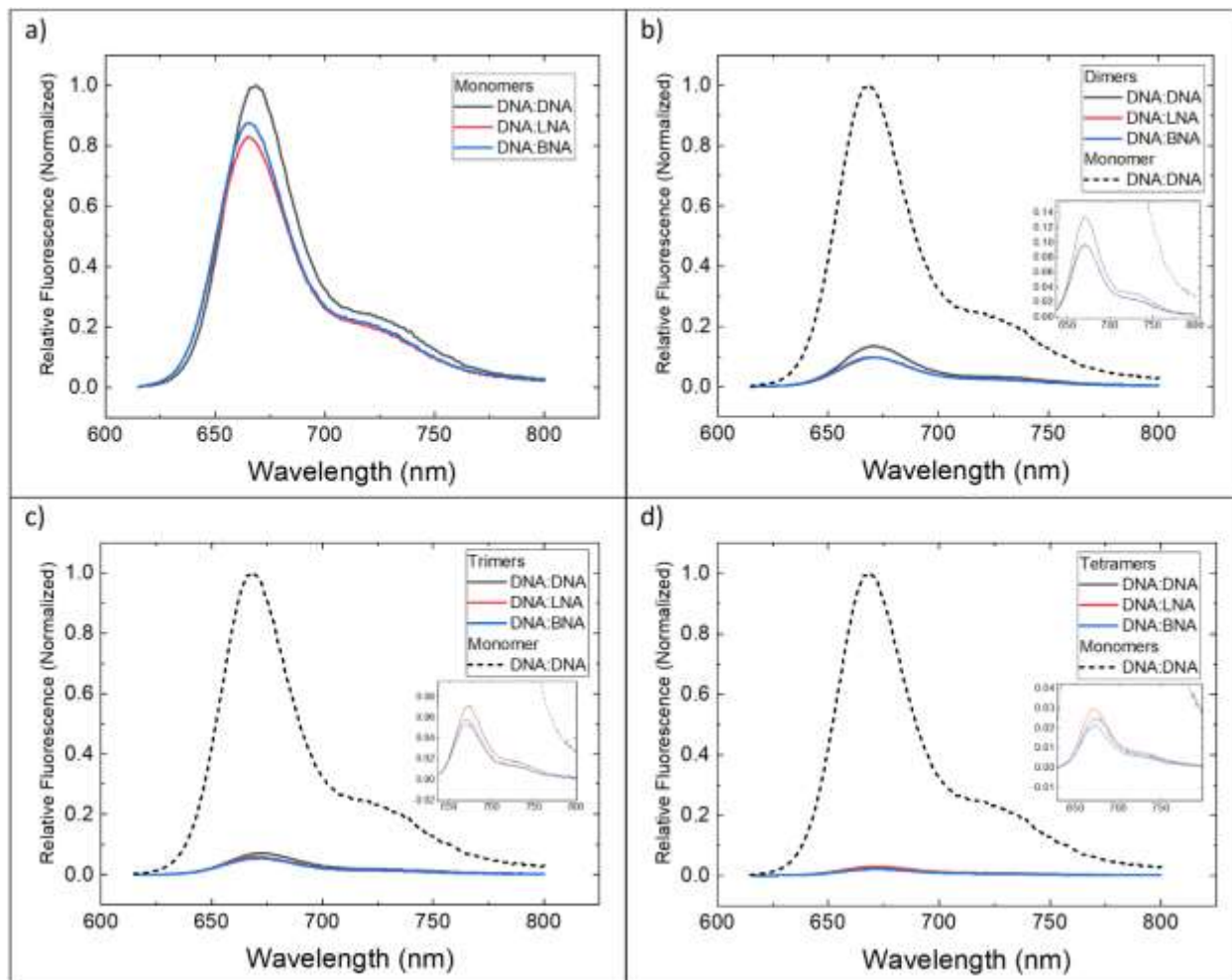


**Figure S31:** Relative fluorescence intensity, normalized with respect to absorbance-corrected monomer fluorescence intensity for **a)** monomers, **b)** dimers, **c)** trimers, and **d)** tetramers templated with DNA:DNA (**black**), DNA:LNA (**red**), and DNA:BNA (**blue**). Insets show aggregate spectra in more detail.

**Acknowledgments:** Molecular graphics images in **Figure S23-S25** were produced using the UCSF Chimera package from the Resource for Biocomputing, Visualization, and Informatics at the University of California, San Francisco (supported by NIH P41 RR-01081)<sup>7</sup>.

## S17: References

- (1) Kühn, O.; Renger, T.; May, V. Theory of Exciton-Vibrational Dynamics in Molecular Dimers. *Chem. Phys.* **1996**, *204*, 99–114. [https://doi.org/10.1016/0301-0104\(95\)00448-3](https://doi.org/10.1016/0301-0104(95)00448-3).
- (2) Holstein, T. Studies of Polaron Motion. Part I. The Molecular-Crystal Model. *Ann. Phys. (N. Y.)*. **1959**, *8*, 325–342. [https://doi.org/10.1016/0003-4916\(59\)90002-8](https://doi.org/10.1016/0003-4916(59)90002-8).
- (3) Abramavicius, D.; Palmieri, B.; Mukamel, S. Extracting Single and Two-Exciton Couplings in Photosynthetic Complexes by Coherent Two-Dimensional Electronic Spectra. *Chem. Phys.* **2009**, No. 357(1-3), 79–84.
- (4) Abramavicius, D.; Palmieri, B.; Voronine, D. V.; Šanda, F.; Mukamel, S. Coherent Multidimensional Optical Spectroscopy of Excitons in Molecular Aggregates; Quasiparticle versus Supermolecule Perspectives. *Chem. Rev.* **2009**, *109*, 2350–2408. <https://doi.org/10.1021/cr800268n>.
- (5) Hestand, N. J.; Spano, F. C. Molecular Aggregate Photophysics beyond the Kasha Model: Novel Design Principles for Organic Materials. *Acc. Chem. Res.* **2017**, *50*, 341–350. <https://doi.org/10.1021/acs.accounts.6b00576>.
- (6) Czikkely, V.; Forsterling, H. D.; Kuhn, H. Extended Dipole Model for Aggregates of Dye Molecules. *Chem. Phys. Lett.* **1970**, *6*, 207–210. [https://doi.org/10.1016/0009-2614\(70\)80220-2](https://doi.org/10.1016/0009-2614(70)80220-2).
- (7) Pettersen, E. F.; Goddard, T. D.; Huang, C. C.; Couch, G. S.; Greenblatt, D. M.; Meng, E. C.; Ferrin, T. E. UCSF Chimera - A Visualization System for Exploratory Research and Analysis. *J. Comput. Chem.* **2004**, *25*, 1605–1612. <https://doi.org/10.1002/jcc.20084>.
- (8) Huang, K.; Rhys, A. Theory of Light Absorption and Non-Radiative Transitions in F-Centres; **1950**; pp 74–92. [https://doi.org/10.1142/9789812793720\\_0007](https://doi.org/10.1142/9789812793720_0007).
- (9) Berova, N.; Di Bari, L.; Pescitelli, G. Application of Electronic Circular Dichroism in Configurational and Conformational Analysis of Organic Compounds. *Chem. Soc. Rev.* **2007**, *36*, 914–931. <https://doi.org/10.1039/b515476f>.
- (10) Kypr, J.; Kejnovská, I.; Bednářová, K.; Vorlíčková, M. Circular Dichroism Spectroscopy of Nucleic Acids. In *Compr. Chiroptical Spectrosc. Appl. Stereochem. Anal. Synth. Compd. Nat. Prod. Biomol.*; Wiley, **2012**; pp 575–586. <https://doi.org/10.1002/9781118120392.ch17>.
- (11) WebPlotDigitizer - Copyright 2010-2020 Ankit Rohatgi <https://apps.automeris.io/wpd/> (accessed 2021 -06 -21).
- (12) Ivanova, A.; Rösch, N. The Structure of LNA:DNA Hybrids from Molecular Dynamics Simulations: The Effect of Locked Nucleotides. *J. Phys. Chem. A* **2007**, *111*, 9307–9319. <https://doi.org/10.1021/jp073198j>.